
Two- sided turbulent surface layer parameterizations for computing air- sea fluxes

Pelletier Charles ^{1,2,*}, Lemarie Florian ¹, Blayo Eric ¹, Bouin Marie-Noelle ^{3,4}, Redelsperger Jean-Luc ⁴

¹ Univ. Grenoble Alpes, Inria, CNRS, Grenoble INP, LJK, 38000 Grenoble, France

² Earth and Life Institute, UCLouvain, Louvain-la-Neuve, Belgium

³ CNRM, Météo-France/CNRS, Université de Toulouse, France

⁴ Univ. Brest, CNRS, IRD, Ifremer, Laboratoire d'Océanographie Physique et Spatiale (LOPS), IUEM, Brest, France

* Corresponding author : Charles Pelletier, email address : charles.pelletier@uclouvain.be

Abstract :

Standard methods for determining air - sea fluxes typically rely on bulk algorithms set in the frame of Monin-Obukhov stability theory (MOST), using ocean surface fields and atmosphere near-surface fields. In the context of coupled ocean - atmosphere simulations, the shallowest ocean vertical level is usually used as bulk input and by default, the turbulent closure is one-sided: it extrapolates atmosphere near-surface solution profiles (for wind speed, temperature and humidity) to the prescribed ocean surface values. Using near-surface ocean fields as surface ones is equivalent to considering that in the ocean surface layer, solution profiles are constant instead of also being determined by a turbulent closure. Here we introduce a method for extending existing turbulent parameterizations to a two-sided framework by explicitly including the ocean surface layer within the aforementioned parameterizations. The formalism we use for this method is derived from that of classical turbulent closures, so that our novelties can easily be implemented within existing formulations. Special care is taken to ensure the smoothness of resulting solution profiles. Other physical phenomena, such as the penetration of radiative fluxes in the ocean and the formation of waves, are then included within our formalism, and their effects are assessed. We also investigate the impact of such two-sided bulk formulations on air - sea fluxes evaluated from a setting similar to those of coupled ocean - atmosphere simulations.

Keywords : Turbulent parameterizations, air-sea fluxes, bulk formulae, ocean surface layer, numerical methods, ocean-atmosphere coupling

9 sea interactions play a crucial role for the evolution of the Earth system at both meteorological (e.g. Emanuel,
10 1986) and climatological (e.g. Neelin et al., 1992) scales. In climate models, the interactions between these Earth
11 system components are primarily conveyed through the exchange of momentum, mass and heat fluxes. A significant
12 part of these fluxes is linked to turbulent processes in the surface layer (SL) of the atmosphere and ocean, roughly
13 defined as between 1 m below and 10 m above their common interface. The specific physical processes of the SL are

14 central in determining turbulent air-sea fluxes, which are then used as boundary conditions for ocean and atmosphere
15 models. The procedures for obtaining turbulent air-sea fluxes from large-scale quantities (extractable from climate
16 models) are referred to as bulk closures (e.g. Fairall et al., 2002; Large, 2006). Consequently, establishing an adequate
17 parameterization of the SL between the atmosphere and ocean has been a steady point of interest for the development
18 of numerical weather and climate prediction models.

19 The overwhelming majority of air-sea SL parameterization schemes are expressed in the framework of Monin-Obukhov
20 similarity theory (MOST, Monin and Obukhov, 1954) applied to the near-surface atmosphere. While additional phys-
ical effects have gradually been included within SL parameterizations, the fundamental hypotheses at their core have
21 persisted: the atmosphere SL is described by the constant flux layer approximation, resulting from a combination of
22 “law of the wall” and buoyancy effects, which calls for characterizing the surface roughness and column stability. Air-
23 sea fluxes parameterizations have mostly been designed for atmosphere circulation models, assuming ocean surface
24 properties to be known. However, over the last decades, several ocean-specific processes have been progressively
25 integrated within flux computations.
26

27 Sellers (1967) first distinguished subsurface temperatures (at depth $O(1\text{ m})$) from skin temperature (at depth $O(1\text{ cm})$),
28 the latter being relevant for assessing the upward longwave, sensible and latent heat air-sea fluxes. Donlon et al. (2002)
29 established a classification of near-surface ocean temperature measurements, insisting that measured temperatures
30 are instrument-dependent, e.g. on the depth of the probe used for field measurements or on the wavelength used
31 in radiometry. Ward et al. (2004) and Ward (2006) performed field measurements of the “skin” temperature layer,
32 showing that assimilating it to the subsurface one could yield errors on the air-sea heat fluxes in the order of 10 to
33 50 W/m^2 . In parallel, additional parameterizations were included within bulk closures to account for such effects (e.g.,
34 Fairall et al., 1996; Zeng and Beljaars, 2005; Bellenger et al., 2017).

35 The wind stress dependency to surface currents has originally been neglected in bulk closures. However, both nu-
36 merical experiments (Pacanowski, 1987; Duhaut and Straub, 2006; Dawe and Thompson, 2006; Renault et al., 2016)
37 and flux measurements (Kelly et al., 2001) have shown that surface currents bear an impact on air-sea fluxes. More
38 recently, the effects of this wind stress modulation on coupled ocean - atmosphere have been investigated (Renault
39 et al., 2019a), and turned out to have a non-negligible impact on the energetics in coupled simulations (Renault et al.,
40 2019b).

41 The parameterizations listed above are all part of a community effort to include the influence of ocean-specific pro-
42 cesses within surface layer parameterizations. In this paper, our objective is to develop a general method for adding
43 a simple representation of the ocean near-surface layer within existing bulk closures. The main idea is to extend a
44 given one-sided bulk formulation to account for the evolution of currents and temperature, by extrapolating them
45 from the depth at which the ocean information is available up to the surface, as shown in Fig. 1. At first, our approach
46 is built in a very idealized framework. However, the formalism is flexible enough to seamlessly include additional or
47 alternative parameterizations, such as the effects of waves of air-sea momentum exchanges and the potential wind
48 stress deflection resulting from it.

49 The paper is organized as follows. Section 2 briefly introduces existing bulk closures and underlines their limitations
50 in a coupled ocean-atmosphere context. Section 3 introduces a slight modification on atmosphere bulk closures,
51 allowing them to explicitly treat the air-sea interface. In Sec. 4, an idealized parameterization for the ocean SL is
52 introduced, solely accounting for shear turbulence. In Sec. 5, the inclusion of some specific non-turbulent phenomena
53 within this framework (effects of waves and of radiation penetration) are discussed, thus illustrating its flexibility.

54 Section 6 investigates the effects of our novelty of offline turbulent flux computations. Finally, concluding remarks
 55 and perspectives are given in Sec. 7.

56 2 | EXISTING BULK CLOSURES AND THEIR LIMITATIONS IN A COUPLED 57 CONTEXT

58 Throughout this paper, local horizontal homogeneity is assumed. Our study is therefore set in a 1D air-sea column
 59 configuration. z , the vertical coordinate, is orientated upwards, with the mean sea level assumed flat and defined
 60 by $\{z = 0\}$. Therefore, $z < 0$ in the ocean and $z > 0$ in the atmosphere. The index $\alpha \in \{o, a\}$ distinguishes
 61 ocean and atmosphere variables. The physical variables of interest are the horizontal velocity $u \in \mathbb{R}$ and the potential
 62 temperature $\theta \in \mathbb{R}_+^*$. The atmosphere is assumed to be dry, and latent heat resulting from mass exchanges is neglected.
 63 This physically limiting assumption is made for easing the formulation of our framework. Moisture effects can be
 64 implicitly included by considering virtual potential temperatures, and latent heat can be explicitly included by treating
 65 the moisture profiles in the same manner as temperature ones. While u is assumed always aligned in the same direction,
 66 Section 5.1 investigates the effects of 2D horizontal velocities on the potential deflection of surface stress from near-
 67 surface winds. The letter x will be used as a general notation for either u or θ . Our focus is on the surface layer (SL),
 68 defined for each variable as the $]z_o^1; z_a^1[$ interval, with $z_o^1 < 0 < z_a^1$. Typically, $z_o^1 \approx -1$ m and $z_a^1 \approx 10$ m correspond
 69 to the heights at which the information is extracted from the vertical finite-difference scheme of each model. These
 70 values of z_o^1 and z_a^1 are used in all numerical examples below. The SL is nested within the ocean-atmosphere boundary
 71 layer, being roughly 10 times thinner. In forced or coupled numerical simulations, it corresponds to the layer which
 72 is not covered by the vertical discretization of the considered model (ocean or atmosphere). Table 1 contains a non-
 73 exhaustive list of mathematical symbols introduced in this paper.

74 2.1 | Air-sea turbulent fluxes and their relationship to SL solution profiles

75 This section is intended for general readers to recall the basic aspects about the derivation of bulk formulations nec-
 76 essary for the proper understanding of our approach. The boundary conditions enforced to the atmosphere at $z = z_a^1$
 77 are:

$$78 \mathcal{K}_{a,u} \partial_z u = \tau / \rho_a \quad (1a)$$

$$79 \mathcal{K}_{a,\theta} \partial_z \theta = Q^H / (\rho_a c_a^p) \quad (1b)$$

80 where $\mathcal{K}_{a,u}$ is the momentum diffusivity; $\mathcal{K}_{a,\theta}$ is the thermal diffusivity; τ is the wind stress; ρ_a is the atmosphere
 81 density; Q^H is the sensible heat flux; c_a^p is the dry atmosphere heat capacity. In Equation 1, ρ_a and c_a^p are assumed
 82 constant and known. τ and Q^H are turbulent fluxes to be determined. Both diffusivities $\mathcal{K}_{a,x}$ also depend on tur-
 83 bulent scales, and thus need to be parameterized. In the atmosphere SL, the relevant turbulent scales for velocity
 84 and temperature are $u_a^* > 0$ and θ_a^* , respectively. Formally, MOST states that the atmosphere SL contains a “purely
 85 turbulent” sublayer (grey shading in Fig. 1), above the direct influence of surface roughness and below the heights
 86 at which non-turbulent processes (e.g. pressure gradients, Coriolis effect) become important. In this layer of MOST
 87 validity, (u_a^*, θ_a^*) can be linked to $(\partial_z u, \partial_z \theta)$ by building dimensionless groups and applying the π -theorem (Buckingham,

1914). Throughout this manuscript, we assume z_a^1 to be within the layer of MOST validity. Practically, this implies that Equation 1 holds on this part of the SL, with both diffusivities given by:

$$\mathcal{K}_{a,u}^{MO}(z) = \frac{\kappa u_a^* z}{\phi_a^m(z/L_a)} \quad (2a)$$

$$\mathcal{K}_{a,\theta}^{MO}(z) = \frac{\kappa u_a^* z}{\phi_a^h(z/L_a)} \quad (2b)$$

where $\kappa \approx 0.4$ is the von Kármán constant. $L_a = (u_a^*)^2 \theta(z_a^1) / (g \kappa \theta_a^*)$, where $g \approx 9.81$ m/s², is a signed characteristic length (Obukhov, 1971) rendering the fluid stratification's effect on $\mathcal{K}_{a,x}^{MO}$ through the two stability functions (ϕ_a^m, ϕ_a^h) (e.g. Businger et al., 1971). From dimensional analysis, τ and Q^H can be scaled as $\tau = \rho_a (u_a^*)^2$ and $Q^H = \rho_a c_a^p u_a^* \theta_a^*$. From now on, we also assume that the SL is a constant flux layer, hence u_a^* and θ_a^* are constant as well. Combining the dimensionless groups with the constant flux assumption, by injecting Equation 2 into Equation 1 and integrating with respect to z yields:

$$\llbracket u \rrbracket_0^{z_a^1} = \frac{u_a^*}{\kappa} \left[\ln \left(\frac{z_a^1}{z_{a,u}^r} \right) - \psi_a^m \left(\frac{z_a^1}{L_a} \right) \right] \quad (3a)$$

$$\llbracket \theta \rrbracket_0^{z_a^1} = \frac{\theta_a^*}{\kappa} \left[\ln \left(\frac{z_a^1}{z_{a,\theta}^r} \right) - \psi_a^h \left(\frac{z_a^1}{L_a} \right) \right] \quad (3b)$$

where $\llbracket x \rrbracket_{z_1}^{z_2} := x(z_2) - x(z_1)$ and (ψ_a^m, ψ_a^h) are the integrated forms of the stability functions (Paulson, 1970). In the following, for the sake of conciseness, we assume that the atmosphere information is available at the same height z_a^1 for both u and θ . Equation 3 most notably introduces $(z_{a,u}^r, z_{a,\theta}^r)$, a set of two roughness heights, which are used as lower integration boundaries of the invariant dimensionless groups constituted by Equation 1. Indeed, physically, phenomena unrelated to MOST such as surface roughness are expected to dominate in the direct vicinity of the surface; mathematically, Equation 1 with $\mathcal{K}_{a,x}$ given by Equation 2 is not integrable down to $z = 0$. Hence the introduction of roughness heights, which can be defined as the heights at which MOST-derived profiles (of u or θ) reach their respective surface values. In that regard, Equation 3 can be understood as an integration of idealized MOST profiles rather than the actual physical profiles, which are not known as $z \rightarrow 0$. In Equation 3, the surface is assimilated to the roughness heights, so its left members are defined as $\llbracket x \rrbracket_0^{z_a^1}$ instead of $\llbracket x \rrbracket_{z_{a,x}^r}^{z_a^1}$. Equation 3 corresponds to classical "law of the wall" profiles (the logarithm term) perturbed by a stability-rendering term (the ψ_a^x term). Over the ocean, the stability at roughness heights can be neglected as $z_{a,x}^r \ll z_a^1$, and $\psi_a^x(\zeta) \xrightarrow{\zeta \rightarrow 0} 0$.

Air-sea fluxes can be determined from Equation 3 by parameterizing $z_{a,u}^r$ and $z_{a,\theta}^r$ as functions of u_a^* (e.g. Smith, 1988; Fairall et al., 2002). Equation 3 can then be exploited as a set of two nonlinear equations on (u_a^*, θ_a^*) . Solving it, usually through a carefully initialized fixed-point algorithm, leads to τ and Q^H , as they are defined from u_a^* and θ_a^* . This procedure is usually referred to as a bulk algorithm. Outside of a few exceptions (e.g. Louis, 1979; Dubrulle et al., 2002), in their vast majority, the theoretical basis of bulk closures is the MOST formalism described above, and their practical implementations arise from parameterizing the roughness heights and stability functions.

2.2 | Limitation on the use of classical bulk closures in a coupled context

Bulk closures described as in Sec. 2.1 have been developed in the framework of atmosphere-only simulations, with ocean surface properties given as external forcings. Such simulations are usually carried with prescribed sea surface

121 temperature (SST) and neglected sea surface currents since in most cases $|u(z=0)| \ll |u(z_a^1)|$. Using bulk closures
122 with these assumptions is consistent with field turbulent flux measurements, which are assessed at heights $z \approx z_a^1$
123 above the ocean, from “skin” surface temperature (at depth $z \approx -1$ cm), unless an explicit parameterization is used
124 (e.g. a cool skin parameterization such as Fairall et al., 1996). Since the closures include a representation of a vertical
125 coordinate z_a^1 , they can be used for both measuring turbulent fluxes (matching the measurement height), and for com-
126 puting them in numerical models, with adapting z_a^1 from context. As a consequence, when using transfer-coefficient
127 based bulk closures (e.g. Large, 2006), atmosphere-model extracted values for u and θ are shifted to reference height
128 levels, through MOST-derived invariant groups, in order to match parameterizations calibrated from observations. In
129 other words, classical bulk closures as described in Sec. 2.1 are expressed with a dependency on a reference height,
130 so that the resulting fluxes are independent from it. In practice, this ensures that in the limits of MOST, air-sea fluxes
131 resulting from classical bulk closures do not depend on the atmosphere model’s vertical discretization.

132 To our understanding, directly extending (i.e. without near-surface parameterizations such as warm layers) classi-
133 cal bulk closures to a forced-ocean or coupled context yields inconsistencies, mostly related to the method (or lack
134 thereof) used for incorporating near-surface ocean fields as bulk closure inputs. Unlike atmosphere-only simulations,
135 in most coupled ones, the shallowest ocean informations available, usually located at a depth of $z_o^1 \approx -1$ m, is directly
136 used as ocean surface information. This is equivalent to assuming that velocity (current) and temperature profiles
137 within the ocean SL are constant with respect to z . Therefore, the depth at which the ocean information used as bulk
138 input is taken does not have any influence on the formulation of the bulk closure. As a consequence, in forced-ocean
139 or coupled experiments, turbulent fluxes arising from classical bulk closures are tributary to the vertical discretization
140 of the ocean model. For example, carrying two “perfect ocean model” experiments with different near-surface vertical
141 discretizations would yield distinct turbulent air-sea fluxes, which can be problematic.

142 In the following, we aim at building a formulational framework within which cross-medium bulk closures, more adapted
143 to the context of coupled air-sea simulations, could be expressed. In particular, our formalism allows for vertical shifts
144 to be performed within the ocean SL, so that the resulting bulk closures are depth-input dependent, in the same way
145 classical ones are atmosphere height-input dependent. By design, the obtained air-sea fluxes would then be more
146 robust and independent from the discretization of the ocean model.

147 | A SLIGHT ADAPTATION OF THE ATMOSPHERE BULK FORMULATION

148 In this section, we prepare our framework by revisiting atmosphere-only bulk closures. Below it is assumed that the
149 surface currents are zero (i.e., $u(0) = 0$) and that the potential temperatures at $z = z_a^1$ and $z = 0$ are known and
150 used as inputs. Assuming surface properties to be known is an idealization, as such information cannot be measured
151 (Donlon et al., 2002; Kent et al., 2017). A discussion on circumventing this issue is proposed in appendix B. Our
152 objective here is to build a bulk closure which results from integrating solution profiles within the atmosphere surface
153 layer (ASL) from the reference z_a^1 height, down to the ocean - atmosphere interface ($z = 0$), instead of the traditional
154 nonzero “roughness heights”, so to get a direct connection to the underlying ocean. As in typical MOST applications,
155 we assume the ASL to be a constant flux layer. Our bulk closure is thus based on integrating dimensionless groups

156 with the following diffusivities, slightly adapted from Equation 2:

$$157 \quad \mathcal{K}_{a,u}^{ad}(z) = \frac{\kappa u_a^* z + \mathcal{K}_{a,u}^V}{\phi_a^m(z/L_a)} \quad (4a)$$

$$158 \quad \mathcal{K}_{a,\theta}^{ad}(z) = \frac{\kappa u_a^* z + \mathcal{K}_{a,\theta}^V}{\phi_a^h(z/L_a)} \quad (4b)$$

159 where $\mathcal{K}_{a,u}^V, \mathcal{K}_{a,\theta}^V > 0$ is a set of two constant diffusivities, which are to be determined. Their objective is to represent
 160 the molecular effects which dominate over the turbulent ones in the viscous sublayers, as $z \rightarrow 0$. In Equation 4,
 161 they are divided by stability functions for convenience. The dimensionless groups arising from Equations 1 and 4 are:

$$162 \quad \partial_z u = \frac{(u_a^*)^2}{(\kappa u_a^* z + \mathcal{K}_{a,u}^V) / \phi_a^m(z/L_a)} \quad 0 \leq z \leq z_a^1 \quad (5a)$$

$$163 \quad \partial_z \theta = \frac{u_a^* \theta_a^*}{(\kappa u_a^* z + \mathcal{K}_{a,\theta}^V) / \phi_a^h(z/L_a)} \quad 0 \leq z \leq z_a^1 \quad (5b)$$

164 Mathematically, the inclusion of $\mathcal{K}_{a,u}^V, \mathcal{K}_{a,\theta}^V > 0$ makes the dimensionless groups Equation 5 integrable on $[0; z_a^1]$.
 165 In other words, while classical dimensionless groups are only relevant for describing the purely turbulent part of the
 166 ASL, Equation 5 can describe its entirety, down to $z = 0$. Using state-of-the-art stability functions (e.g., Höögström,
 167 1988), analytical integrated forms of Equations 1 and 4 can be obtained (see appendix A.1). They are however hard
 168 to manipulate. Obtaining simpler forms is possible by assuming:

$$169 \quad \mathcal{K}_{a,u}^V, \mathcal{K}_{a,\theta}^V \ll \kappa u_a^* z_a^1, \kappa u_a^* |L_a| \quad (6)$$

170 which is physically justified, as molecular effects are expected to be negligible compared to: (i) turbulent ones at $z = z_a^1$;
 171 (ii) stability-induced ones. Assuming once again that the SL is a constant flux layer, integrating Equation 5 downwards
 172 from z_a^1 and using Equation 6 yields (see appendix A.2 for proof):

$$173 \quad u(z) = u(z_a^1) - \frac{u_a^*}{\kappa} \left[\ln \left(\frac{z_a^1}{z + \mathcal{K}_{a,u}^V / (\kappa u_a^*)} \right) - \psi_a^m \left(\frac{z_a^1}{L_a} \right) + \psi_a^m \left(\frac{z}{L_a} \right) \right] \quad 0 \leq z \leq z_a^1 \quad (7a)$$

$$174 \quad \theta(z) = \theta(z_a^1) - \frac{\theta_a^*}{\kappa} \left[\ln \left(\frac{z_a^1}{z + \mathcal{K}_{a,\theta}^V / (\kappa u_a^*)} \right) - \psi_a^h \left(\frac{z_a^1}{L_a} \right) + \psi_a^h \left(\frac{z}{L_a} \right) \right] \quad 0 \leq z \leq z_a^1 \quad (7b)$$

175 In particular, assessing Equation 7 at $z = 0$ leads to:

$$176 \quad \llbracket u \rrbracket_0^{z_a^1} = \frac{u_a^*}{\kappa} \left[\ln \left(\frac{z_a^1}{\mathcal{K}_{a,u}^V / (\kappa u_a^*)} \right) - \psi_a^m \left(\frac{z_a^1}{L_a} \right) \right] \quad (8a)$$

$$177 \quad \llbracket \theta \rrbracket_0^{z_a^1} = \frac{\theta_a^*}{\kappa} \left[\ln \left(\frac{z_a^1}{\mathcal{K}_{a,\theta}^V / (\kappa u_a^*)} \right) - \psi_a^h \left(\frac{z_a^1}{L_a} \right) \right] \quad (8b)$$

178 where $\llbracket x \rrbracket_{z_1}^{z_2} = x(z_2) - x(z_1)$. Equation 8 can be used as a bulk closure, i.e. a set of equation on (u_a^*, θ_a^*) , depending
 179 on input fields at $z = 0$ and $z = z_a^1$. Practically speaking, $\mathcal{K}_{a,u}^V$ and $\mathcal{K}_{a,\theta}^V$ can be parameterized so that the Equation 8

181 closure is strictly equivalent¹ to the classical one Equation 3, using roughness heights as lower integration boundaries.
 182 This can be done by setting:

$$183 \quad \mathcal{K}_{a,u}^v = \kappa u_a^* z_{a,u}^r \quad (9a)$$

$$184 \quad \mathcal{K}_{a,\theta}^v = \kappa u_a^* z_{a,\theta}^r \quad (9b)$$

185 In other words, the new ASL closure Equation 8 is transparent in that it only differs from classical ones in terms
 186 of formalism, when assuming surface ocean fields to be known. More adequate tuning for $\mathcal{K}_{a,x}^v$ requires the ocean
 187 surface layer to be treated, and are discussed in appendix B. When perturbing diffusivities with positive constant
 188 factors as in Equation 4, the resulting viscous profiles' asymptotes are logarithmic functions, stopping at an equivalent
 189 roughness height of $\mathcal{K}_{a,x}^v / (\kappa u_a^*)$. It should be underlined that any other type of profiles (as long as they are monotonous
 190 with respect to z) can be generated by relaxing Equation 4 and perturbing $\mathcal{K}_{a,x}^v$ with a carefully built z -dependent
 191 function. However, this endeavor is not pursued here as our objective is to obtain a formalism that simply treats
 192 the full $]0; z_a^1[$ interval, rather than describing the viscous sublayers as accurately as possible. Hence, the viscous
 193 parameterization is kept simple, with a minimal (null here) impact on bulk closure outputs.

194 Using the adapted closure Equation 8 instead of the classical one Equation 3 has three assets. First, it is directly derived
 195 from integrating a dimensionless group down to $z = 0$, instead of using the roughness heights as an arbitrary lower
 196 integration bound. In our opinion, including $\mathcal{K}_{a,x}^v$ (and tuning it through Equation 9) within the effective surface layer
 197 diffusivities is more intuitive than stopping the dimensionless groups' integration at the $z_{a,x}^r$ nonzero heights. Second,
 198 the new closure includes a smooth transition between the turbulent ($z \gg z_{a,x}^r$) and viscous ($z \lesssim z_{a,x}^r$) sublayers of the
 199 ASL. Integrating Equations 1 and 4 from z_a^1 down to $z \in]0; z_a^1[$ allows for a full coverage of the ASL, including the
 200 viscous sublayers which cannot be represented by classical dimensionless groups. As Fig. 2 shows, using the modified
 201 bulk closure allows for smooth profiles to be integrated down to $z = 0$, and leads to negligible differences far from
 202 the viscous sublayers, as soon as $z \gtrsim 10^{-3}$ m. Third, at the expense of physically crude hypotheses on the viscous
 203 sublayers, it permits unambiguously expressing the solution profiles and their derivatives at $z = 0^+$, which will be useful
 204 in the next section.

205 4 | IDEALIZED SYMMETRICAL OCEAN-ATMOSPHERE BULK FORMULATION

206 In this section, our objective is to extend the classical MOST framework so that two-sided ocean - atmosphere closures
 207 can be expressed within it. Strictly speaking, this should be distinguished from deriving new closures: below, we are
 208 not establishing new parameterizations for roughness and/or stability. We are simply proposing a method for vertically
 209 extending existing closures into the ocean. Hence, our novelties are more to be understood in terms of framework
 210 rather than closure in itself. In the following, we assume that the surface current velocity and potential temperature
 211 are known at a reference depth $z_o^1 \approx -1$ m instead of the surface. This setting is similar to that of forced ocean or
 212 coupled ocean - atmosphere simulations, where the shallowest ocean information available is located at a nonzero
 213 depth. Before including more realistic physics in Sec. 5, here we simply extend the formulations of Sec. 3 to build
 214 idealized two-sided ocean-atmosphere bulk closures, aiming at determining turbulent scales from $u(z_o^1)$, $u(z_a^1)$, $\theta(z_o^1)$
 215 and $\theta(z_a^1)$. We refer to the "ocean near-surface layer" (ONSL) as the thin layer located between z_o^1 and $z = 0$, above

¹In the zeroth order limit arising from Equation 6.

216 the shallowest ocean vertical level. The ONSL is much thinner than the ocean boundary layer (OBL), whose depth can
 217 reach up to a few hundreds of meters.

218 | MOST-derived ocean surface layer

219 In this section, the ONSL is idealized and its description is based on the following assumptions (which will all be
 220 gradually relaxed in Sec. 5):

221 **(iONSL-1)** The ONSL is a constant flux layer.

222 **(iONSL-2)** As in the ASL, only turbulence and molecular effects play a role on a the ONSL, i.e. the wave effects and
 223 radiative fluxes are not explicitly represented.

224 **(iONSL-3)** The wind stress and sensible heat fluxes are conserved across the ocean-atmosphere interface.

225 **(iONSL-4)** The near-surface currents $u(z_o^1)$ are perfectly aligned with the near-surface winds $u(z_a^1)$, both being aligned
 with the i -axis, hence $(u(z_o^1), u(z_a^1)) \in \mathbb{R}^2$.

227 (iONSL-1) - (iONSL-4) lead to a rough, purely shear-driven description of the ONSL.

228 The relevancy of such an idealized description has been validated by direct numerical simulations (Tsai et al., 2005),
 229 as well as both laboratory (Wu, 1975, 1984; Mcleish and Putland, 1975) and field (Churchill and Csanady, 1983;
 230 Csanady, 1984) experiments. However, under moderate to strong winds, other sources of air-sea exchanges (such
 231 as wave-induced stress) develop and interplay with purely turbulent and viscous effects. In particular, as soon as
 232 $u_a \geq 3$ m/s, (iONSL-2) becomes physically invalid as waves start playing a crucial role in the momentum transfer to
 233 the ocean. Therefore, the assumptions above are expressed to build our framework, which will be extended in Sec. 5
 234 to account for more realistic parameterizations.

235 As for z_a^1 in Sec. 2, we also assume that z_o^1 , the shallowest ocean level, is located within the domain of MOST va-
 236 lidity. (iONSL-1) and (iONSL-2) thus lead to modelling the ONSL in the same way as the ASL was, through ocean
 237 dimensionless groups analogous to the atmosphere ones Equation 5, for $z_o^1 \leq z \leq 0$:

$$238 \quad \partial_z u = \frac{(u_o^*)^2}{(\kappa u_o^*(-z) + \mathcal{K}_{o,u}^v) / \phi_o^m(-z/L_o)} \quad (10a)$$

$$239 \quad \partial_z \theta = \frac{u_o^* \theta_o^*}{(\kappa u_o^*(-z) + \mathcal{K}_{\theta,o}^v) / \phi_o^h(-z/L_o)} \quad (10b)$$

240 where $u_o^* > 0$ and θ_o^* are ocean turbulent scales; $\mathcal{K}_{o,u}^v, \mathcal{K}_{\theta,o}^v > 0$ ocean molecular viscosity and thermal diffusiv-
 241 ity; ϕ_o^m, ϕ_o^h a set of two stability functions; and L_o the ocean Obukhov length defined as in Large (1998), i.e. $L_o =$
 242 $(u_o^*)^2 / (\kappa g \alpha_{eos} \theta_o^*)$, with $\alpha_{eos} \approx 1.8 \times 10^{-4} \text{ K}^{-1}$ the ocean thermal expansion coefficient. The ϕ_o^x stability functions
 243 can differ from their atmosphere counterparts. In the following, we will use the ocean stability functions from Large

244 et al. (2019):

$$245 \quad \phi_o^m(\zeta) = \phi_o^h(\zeta) = 1 + 5\zeta \quad \zeta \geq 0 \quad (11a)$$

$$246 \quad \phi_o^m(\zeta) = (1 - 14\zeta)^{-1/3} \quad \zeta < 0 \quad (11b)$$

$$247 \quad \phi_o^h(\zeta) = (1 - 25\zeta)^{-1/3} \quad \zeta < 0 \quad (11c)$$

248 The integrated forms of Equation 11b and Equation 11c are given by (for $x \in \{m, h\}$):

$$249 \quad \psi_o^x(\zeta) = \sqrt{3} \left[\text{Arctan}(\sqrt{3}) - \text{Arctan}\left(\frac{\sqrt{3}}{3}(2C_x + 1)\right) \right] + \frac{3}{2} \ln\left(\frac{(C_x)^2 + C_x + 1}{3}\right) \quad (12)$$

250 where $C_m = (1 - 14\zeta)^{1/3}$ and $C_h = (1 - 25\zeta)^{1/3}$.

251 | Turbulent closure for the idealized ONSL

252 In this section, we rely on the hypotheses above to constrain the four new unknown quantities (u_o^* , θ_o^* , $\mathcal{K}_{o,u}^v$ and $\mathcal{K}_{\theta,o}^v$)
253 introduced by Equation 10. First, (iONSL-3) yields:

$$254 \quad u_o^* = \lambda_u u_a^* \quad (13a)$$

$$255 \quad \theta_o^* = \lambda_\theta \theta_a^* \quad (13b)$$

256 where $\lambda_u = \sqrt{\rho_a/\rho_o} \approx 3 \times 10^{-2}$ and $\lambda_\theta = (\sqrt{\rho_a} c_a^p)/(\sqrt{\rho_o} c_o^p) \approx 8 \times 10^{-3}$. Second, unlike classical bulk closures, the
257 adapted ones allow assessing solution profiles at the interface $z = 0$. Across the interface, the gradients of the solution
258 profiles are assumed to satisfy the following molecular constraint:

$$259 \quad (\rho_a \mathcal{K}_a^m \partial_z u)_{z=0^+} = (\rho_o \mathcal{K}_o^m \partial_z u)_{z=0^-} \quad (14a)$$

$$260 \quad (\rho_a c_a^p \mathcal{K}_a^m \partial_z \theta)_{z=0^+} = (\rho_o c_o^p \mathcal{K}_o^m \partial_z \theta)_{z=0^-} \quad (14b)$$

261 where \mathcal{K}_α^m are the kinematic viscosities for $\alpha \in \{o, a\}$ medium: $\mathcal{K}_a^m = 1.5 \times 10^{-5}$ m²/s and $\mathcal{K}_o^m = 10^{-6}$ m²/s. Equa-
262 tion 14 implies that at the interface, the intrinsic properties of each medium determine the slope break of inbetween
263 fluxes. Imposing Equation 14 with Equations 5 and 10 injected yields:

$$264 \quad \mathcal{K}_{o,x}^v = \mu_m \mathcal{K}_{a,x}^v, \quad x \in \{u, \theta\} \quad (15)$$

265 where $\mu_m = \mathcal{K}_o^m/\mathcal{K}_a^m \approx 6.7 \times 10^{-2}$. Equations 13 and 15 introduce four new constraints which bind the four ocean
266 turbulent and molecular quantities to their atmosphere counterparts. Yet, achieving turbulent closure cannot directly
267 be done by transposing Equation 8, as in this section, surface currents and temperature are unknown. This can be
268 overcome by integrating Equation 10 on $[z_o^1; 0]$, with assuming as in Equation 6 that $\mathcal{K}_{o,u}^v, \mathcal{K}_{o,\theta}^v \ll \kappa u_o^*(-z_o^1), \kappa u_o^*|L_o|$,

269 and by injecting Equations 9 and 15:

$$270 \quad \llbracket u \rrbracket_{z_o^1}^0 = \frac{u_o^*}{\kappa} \left[\ln \left(\frac{-z_o^1}{\mu_m \mathcal{K}_{a,u}^{\mathcal{V}} / (\lambda_u \kappa u_a^*)} \right) - \psi_o^m \left(\frac{-z_o^1}{L_o} \right) \right] \quad (16a)$$

$$271 \quad \llbracket \theta \rrbracket_{z_o^1}^0 = \frac{\theta_o^*}{\kappa} \left[\ln \left(\frac{-z_o^1}{\mu_m \mathcal{K}_{a,\theta}^{\mathcal{V}} / (\lambda_u \kappa u_a^*)} \right) - \psi_o^h \left(\frac{-z_o^1}{L_o} \right) \right] \quad (16b)$$

272 Combining Equations 8 and 16, and assuming that u and θ are continuous at the interface (i.e., $u(0^+) = u(0^-)$ and
273 $\theta(0^+) = \theta(0^-)$), which is only relevant with revised closures (as classical ones cannot treat $z = 0$), lead to:

$$274 \quad \frac{\kappa \llbracket u \rrbracket_{z_o^1}^{z_a^1}}{u_a^*} = \ln \left(\frac{z_a^1}{z_{a,u}^r} \right) - \psi_a^m \left(\frac{z_a^1}{L_a} \right) + \lambda_u \left[\ln \left(\frac{-z_o^1}{\mu_m z_{a,u}^r / \lambda_u} \right) - \psi_o^m \left(\frac{-z_o^1}{L_o} \right) \right] \quad (17a)$$

$$275 \quad \frac{\kappa \llbracket \theta \rrbracket_{z_o^1}^{z_a^1}}{\theta_a^*} = \ln \left(\frac{z_a^1}{z_{a,\theta}^r} \right) - \psi_a^h \left(\frac{z_a^1}{L_a} \right) + \lambda_\theta \left[\ln \left(\frac{-z_o^1}{\mu_m z_{a,\theta}^r / \lambda_u} \right) - \psi_o^h \left(\frac{-z_o^1}{L_o} \right) \right] \quad (17b)$$

276 where the terms depending on either u_a^* or θ_a^* are in bold font, $z_{a,x}^r$ are assessed from existing roughness parameter-
277 izations (e.g., Smith, 1988; Fairall et al., 2002). The $\lambda_x[\dots]$ terms in Equation 17, which encapsulate the novelties
278 of two-sided closures, are neglected in the standard ones. Equation 17 can be used as a cross-interface turbulent
279 closure: in other words, it provides a set of two nonlinear equations on u_a^* and θ_a^* for determining them from four
280 large-scale, near-surface quantities: $u(z_o^1)$, $u(z_a^1)$, $\theta(z_o^1)$ and $\theta(z_a^1)$.

281 Unlike classical bulk closures, which are limited to $[z_{a,x}^r; z_a^1]$, the revised atmosphere closure introduced in Sec. 3
282 permits unambiguously describing the surface layer arbitrarily close to the $z = 0$ interface. This asset has been used
283 for enforcing the continuity of solution profiles, and the surface gradient condition Equation 14 at $z = 0$. Hence,
284 although the revised atmosphere SL closure is transparent in terms of bulk outputs, it paved the way for obtaining the
285 two-sided closure Equation 17.

286 Figure 3 represents solutions profiles derived from classical, revised one-sided (derived from Sec. 3) and cross-interface
287 two-sided bulk closures. In this idealized case, cross-interface profiles are expectedly smooth, with sharper gradi-
288 ents very close to the ocean-atmosphere interface, and slope break at $z = 0$, as specified by Equation 14. This is
289 physically relevant as $z = 0$ corresponds to a physical interface. While the ocean contribution to the surface layer
290 variations of θ are barely noticeable (in Fig. 3, $\llbracket \theta \rrbracket_{z_o^1}^0 \approx -0.02 \text{ K} \ll \llbracket \theta \rrbracket_{z_o^1}^{z_a^1}$), those to the variations of u are more preva-
291 lent ($\llbracket u \rrbracket_{z_o^1}^0 \approx 0.2 \text{ m/s} \lesssim \llbracket u \rrbracket_{z_o^1}^{z_a^1}$). This can be explained by the fact that $\lambda_u \approx 3.75 \times \lambda_\theta$. Shear turbulence rendering
292 dominant the SL has a remarkably weaker effect on SST compared to diurnal heating ($\pm 3 \text{ K}$, e.g. Halpern and Reed, 1976;
293 Stuart-Menteth et al., 2003) or even cool-skin effect (-0.2 K , e. g. Saunders, 1967; Fairall et al., 1996). However, two-
294 sided closures lead to $u(z = 0)$ being closer to $u(z_a^1)$ than what one-sided closures would predict. Since the relevant
295 large-scale shear for assessing turbulent fluxes is $\llbracket u \rrbracket_{z_o^1}^{z_a^1}$, two-sided closures will then lead to distinct turbulent fluxes
296 compared to one-sided ones.

297 4.3 | Impact on turbulent fluxes

298 By default, traditional bulk closures neglect $\partial_z u$ and $\partial_z \theta$ in the ONSL. Fig. 4 represents the ONSL's contribution to
 299 $[[u]]_{z_0^1}^{z_a^1}$ and $[[\theta]]_{z_0^1}^{z_a^1}$ using our idealized two-sided parameterization for different stability regimes and $0.5 \text{ m/s} \leq [[u]]_{z_0^1}^{z_a^1} \leq$
 300 6 m/s . Stronger winds are excluded since they would rapidly generate surface waves which are poorly rendered in
 301 this idealized case, and introduced in Sec. 5.2. Figure 4 suggests that the ONSL may account for a few percent of
 302 $[[u]]_{z_0^1}^{z_a^1}$, and about one percent of $[[\theta]]_{z_0^1}^{z_a^1}$. The ocean contribution increases with $[[u]]_{z_0^1}^{z_a^1}$, with the stability playing a bigger
 303 role under weak shear ($[[u]]_{z_0^1}^{z_a^1} \lesssim 3 \text{ m/s}$). In general, the ONSL contribution increases with column stabilization. Hence
 304 the ocean's contribution is relatively more important under unstable stratification compared to stable one. Practically,
 305 Fig. 4 suggests that by using classical bulk closures in coupled simulations, the u and θ differentials considered as bulk
 306 closure inputs are systematically slightly overestimated.

307 Like the revised atmosphere closure, where $\mathcal{K}_{a,x}^v$ had been tuned from $z_{a,x}^r$ so that bulk outputs are unchanged,
 308 using two-sided cross-interface closures has an impact of the resulting turbulent scales (u_a^*, θ_a^*), and thus on the air-sea
 309 turbulent fluxes. This is represented in Fig. 5, which shows that using our two-sided bulk versions leads to dampened
 310 turbulent fluxes. The effect is stronger on wind stress, which was to be expected, since Fig. 3 suggested that two-sided
 311 closures affect velocities more than potential temperatures.

312 The differences in fluxes displayed in Fig. 5 should be understood as the potential error made when using such closures
 313 with ocean inputs at nonzero depth. This does not correspond to an error in classical bulk closures. Since two-sided
 314 bulk closures depend on z_0^1 , they harbor an extra degree of freedom compared to classical closures. Hence the results
 315 obtained from two-sided closures cannot be fully reproduced by one-sided closures, even through retuning. The
 316 results presented above are based on two-sided bulk closures which have been built as extensions of classical ones
 317 under the minimal hypotheses of Sec. 4.2. In particular, the surface roughness of two-sided bulk closures has been
 318 extended from their one-sided counterpart. A longer-term perspective is to recalibrate surface roughness in the
 319 context of two-sided closures. This could be achieved from colocated air-sea turbulent flux measurements, relying on
 320 ocean inputs at nonzero depths, which is well beyond the scope of this paper.

321 Our idealized study has shown that accounting for shear turbulence within the ONSL may have a non-negligible
 322 impact on the representation of surface currents, and a very limited impact on surface temperature. These effects
 323 lead to perceivable changes on wind stress and sensible heat computations. In our idealized context, one way of
 324 transparently representing the ONSL is to rely on two-sided bulk closures, since they account for variations of currents
 325 and temperature due to shear-generated turbulence within the ONSL, and include a dependency to the depth from
 326 which the ocean information is extracted. In that regard, using two-sided closures is equivalent to extrapolating ocean
 327 currents and temperatures from z_0^1 up to the surface, so that the fields considered as bulk formula inputs match what
 328 these formulations have been calibrated from.

329 5 | TOWARDS INCREMENTALLY MORE REALISTIC TWO-SIDED SURFACE 330 LAYER

331 In this section, more elaborated SL physics, rendering processes other than turbulent shear, are included in our two-
 332 sided framework developed in Sec. 4. The objective is to show the flexibility of our framework. Section 5.1 focuses on
 333 the wind deflection with strong currents; Sec. 5.2 on representing the impact of surface waves; Sec. 5.3 on including

334 radiative fluxes within the ONSL.

335 5.1 | Velocity profile deflection under misaligned winds and currents

336 Throughout Sec. 4 near-surface winds and surface currents were assumed aligned with the i -axis and $\llbracket u \rrbracket_{z_0}^{z_a^1}$ was a scalar
 337 quantity. Relaxing this hypothesis can be carried out by representing 2D horizontal vectors as complex numbers, i.e.
 338 $\llbracket u \rrbracket_{z_0}^{z_a^1} = \left(\llbracket u \rrbracket_{z_0}^{z_a^1} \right)_i + i \left(\llbracket u \rrbracket_{z_0}^{z_a^1} \right)_j \in \mathbb{C}$. Unlike other studies (e.g. Bressan and Constantin, 2019), here we assume the
 339 correlation between wind and near-surface currents to be known and given as an input. Our objective is then to
 340 investigate the velocity's rotation in the (i, j) plane, focus on the direction of the surface currents and its influence on
 341 wind stress.

342 In a 2D context, assuming that the SL is a constant flux layer implies conservation of wind stress in both amplitude
 343 and direction. $\partial_z u$ is always co-aligned with τ in either side of the interface. Let us call $\varphi_\tau \in [-\pi; \pi]$ this direction.
 344 Integrating $\partial_z u$ between any pair $(z_1, z_2) \in [z_0^1; z_a^1]^2$ so that $z_1 < z_2$, yields:

$$\text{Arg} \left(\llbracket u \rrbracket_{z_1}^{z_2} \right) = \varphi_\tau \quad \forall (z_1, z_2) \in [z_0^1; z_a^1]^2 \text{ so that } z_1 < z_2 \quad (18)$$

346 Equation 18 means that if $\partial_z u$ is always aligned with τ , then so is the velocity shear between any z -increasing pair of
 347 vertical levels located within the SL, regardless of the chosen pair. In particular, Equation 18 implies that the stress
 348 directions obtained from relative-winds one-sided and two-sided closures are identical, as $\text{Arg} \left(\llbracket u \rrbracket_{z_0}^{z_a^1} \right) = \text{Arg} \left(\llbracket u \rrbracket_0^{z_a^1} \right) =$
 349 $\text{Arg} \left(\llbracket u \rrbracket_{z_0}^{z_a^1} \right)$. In other words, within a constant flux layer, the sampling heights of velocities (currents or winds) have no impact
 350 on the stress direction, as long as shear is considered. However, including the shear direction (whatever sampling
 351 heights it comes from) does have an impact on wind stress norm and direction, in comparison with bulk closures
 352 relying on absolute winds. Both velocity subgroups Equation 5a and Equation 10a can be rewritten as:

$$\partial_z u = \frac{(u_\alpha^*)^2 e^{i\varphi_\tau}}{(\kappa u_\alpha^* |z| + \mathcal{K}_{o,u}^v) / \phi_\alpha^m (|z|/L_\alpha)} \quad (19)$$

354 for $z \in (0; z_\alpha^1)$ and $\alpha \in \{o, a\}$. Equation 19 can then be integrated to obtain a two-sided closure similar to Equa-
 355 tion 17a, with the left member substituted by $\left| \llbracket u \rrbracket_{z_0}^{z_a^1} \right|$, which should not be mistaken with neither $\llbracket u \rrbracket_{z_0}^{z_a^1}$ nor $\llbracket u \rrbracket_{z_0}^{z_a^1}$.

356 Figure 6 illustrates the impact of shear direction in an extreme case, under neutral stratification ($\llbracket \theta \rrbracket_{z_0}^{z_a^1} = 0$), weak winds
 357 ($u(z_a^1) = 2$ m/s) and relatively strong currents ($u(z_0^1) = 0.5$ m/s). In this experiment, $u(z_a^1)$ is always coaligned with the
 358 i -direction, with the near-surface current direction varying on $[0; \pi]$. Expectedly, Fig. 6a shows that the wind stress
 359 norm increases with the wind-current misalignment. Figures 6b-6c display solution profiles within the ASL: both vector
 360 coordinates progressively adapt to the different near-surface velocity. In Figs. 6b and 6c, the distances between the
 361 solution profiles as $z \rightarrow 0$, and the $(u_i(z_0^1), u_j(z_0^1))$ values (thin vertical lines) highlight the impact of two-sided closures
 362 on velocity directions. With classical closures, all solution profiles would converge towards $(u_i(z_0^1), u_j(z_0^1))$; with two-
 363 sided ones, it only does so if winds and currents are aligned (i.e. $\text{Arg} u(z_0^1) = 0$, red line). As previously mentioned, the
 364 parameters used for Fig. 6 have been set to extreme values, with a low wind-currents ratio ($|u(z_a^1)|/|u(z_0^1)| = 4$), for
 365 didactical purposes and readability. Typical situations are in the $|u(z_a^1)|/|u(z_0^1)| \approx 30$ regime (Wu, 1983), where the

366 impact of currents direction on $|\tau|$ is of the order of a few percents.

367 5.2 | Impact of waves on adapted bulk closures

368 In this section, the impact of waves within our adapted bulk closures is discussed. Under moderate to strong winds
 369 ($U_{10} \geq 3$ m/s), waves develop on the sea surface and Langmuir turbulence is generated within the upper ocean. Both
 370 processes affect the air - sea momentum exchanges. As a consequence, a wave boundary layer (WBL) is generated,
 371 where the velocity profiles are dependent on both turbulence and wave-induced stresses. In this paper, our focus
 372 is on the air-sea surface layer, defined as roughly the top 1 m of the ocean and the bottom 10 m of the atmosphere.
 373 While the atmosphere WBL is nested within our region of interest, as soon as significant waves develop, the ocean
 374 WBL spans outside our region of interest. Hence, an investigation on the effect of waves on our adapted bulk closures
 375 is needed.

376 Prior to carrying on, it should be clarified that the scientific question we want to address here is not as broad as that
 377 on the effects of waves on the full ocean boundary layer, whose depth is typically $O(10 - 100$ m), and the adequate
 378 parameterization for rendering them (see Esters et al., 2018; Li et al., 2019, for reviews). Our focus is on the extrap-
 379 olation of ocean values from $z_o^1 \approx -1$ m up to the surface from a MOST-derived formalism. The scientific question we
 380 want to address is: assuming $u(z_o^1)$ known (which potentially includes Stokes drift contributions), how can the MOST
 381 formalism be further adapted to account for an ONSL perturbed by waves, and what is the subsequent impact on
 382 the wind-induced stress τ ? In other words, we are focusing on the interplay between wave-generated momentum
 383 shear-driven turbulence within the direct vicinity of the ocean surface. To answer this question, we first make a
 384 comment on the implicit rendition of waves by existing parameterizations (Sec. 5.2.1); then, we investigate the impact of
 385 wave-induced momentum stress on our adapted closures (Sec. 5.2.2).

386 5.2.1 | On the default and implicit inclusion of wave effects within bulk closures

387 By default, all bulk closures include the effects of waves, at least to a minimal extent. Indeed, surface layer parameteri-
 388 zations used within bulk closures have been calibrated from field measurements, which may already partly incorporate
 389 the effects of waves. For example, the roughness height $z'_{a,u}$ is directly affected by the presence of waves; this can be
 390 tuned via the Charnock parameter (Kitaigorodskii, 1965). Its piecewise linear definition in the COARE bulk formula
 391 (Fairall et al., 2002) is one example: without prior knowledge of current wave state, it aims at representing the impact
 392 of wind-generated waves. Donelan (1982); Geernaert et al. (1987); Johnson et al. (1998); Taylor and Yelland (2001);
 393 Oort et al. (2002); Drennan et al. (2003) all propose more sophisticated examples of such parameterizations, with
 394 the Charnock parameter usually depending on the wave age c_p^w / u_a^* , where c_p^w is the wave phase speed at its peak
 395 frequency.

396 Accounting for waves within SL parameterization can be further carried out by adapting the effective viscosities $\mathcal{K}_{o,x}$.
 397 Williams and Sullivan (2000) proposed:

$$398 \quad \mathcal{K}_{o,x}^{La} (z) = \mathcal{K}_{o,x}(z) \sqrt{1 + c_w \text{La}^{-4}} \quad (20)$$

399 where $c_w = 0.08$. $\text{La} = \sqrt{u_o^* / u_{stk}}$ is the Langmuir number (its typical range is $0.2 \leq \text{La} \leq 0.7$), with u_{stk} the Stokes drift

at the surface. While more elaborate diagnoses have also been implemented, derived from Equation 20 (e.g. Smyth et al., 2002) or resulting from large-eddy simulations (Large et al., 2019), in the following we will retain Equation 20 as our framework aims at being applicable for climate models run at coarse resolutions, where Stokes drift is not necessarily available. u profiles in the ONSL with the diffusivities defined by Equation 20 are shown in Fig. 9. The middle panels of Fig. 9 show that the surface velocities derived from Equation 20 (“Langmuir”, dotted lines) are slightly closer to $u(z_a^1)$ than the classical ones (“no wave”, full lines). As a result, using Equation 20 comparatively decreases the shear $\left| \left[[u]_0^{z_a^1} \right] \right|$ and both friction velocities u_{α}^* , in agreement with other results from large eddy simulations (e.g. McWilliams et al., 1997) or simplified models (e.g. Teixeira, 2018).

2 | Effects of additional wave-induced ocean momentum input on bulk closures

In this section, we investigate the impact of an additional surface stress linked to the presence of waves, denoted τ_w , considered here as an external momentum source term. We now consider that the effective stress in the ONSL

$$\tau_{o,eff} = \tau + \tau_w \quad (21)$$

In numerical simulations, τ_w could be assessed by an external wave model and sent to the ocean as an additional boundary condition. To our understanding, the impact of injecting τ_w on τ depends on the choice of bulk closure:

- *One-sided absolute-winds bulk closures*: no impact. Currents are completely neglected, which implies that regardless of τ_w and $u(z \leq 0)$, the resulting τ stress remains the same.
- *One-sided relative-winds bulk closures*: indirect impact. The integration of τ_w in the ocean momentum boundary condition has an impact on $u(z_o^1)$, which is assumed equal to $u(z = 0)$, which is itself used as bulk input, hence τ is indirectly impacted.
- *Two-sided bulk closures*: both direct and indirect impacts. In addition to the impact presented above, the ocean velocity dimensionless group Equation 10a is affected by τ_w , as the relevant momentum flux describing the ONSL becomes $\tau + \tau_w$. This in turn leads to a different velocity closure, hence an additional direct impact of waves on τ , which emerges because the ONSL is treated with a dimensionless momentum group.

In the following, the direct impact referred in the last point above is investigated. Using Equation 21 implies that in the ONSL, $\partial_z u$ is aligned with $\tau_{o,eff}$, which can be misaligned with τ . As a consequence, wind stress is not necessarily aligned with $\left[[u]_0^{z_a^1} \right]$: it can be deflected when crossing the air-sea interface. Such phenomena have already been observed in the field (Geernaert, 1988; Geernaert et al., 1993; Grachev et al., 2003; Chen et al., 2018) and obtained from large-eddy simulations (Large et al., 2019; Patton et al., 2019). We define $(\varphi_a, \varphi_o, \varphi_w) \in [-\pi; +\pi]^3$ the directions of the atmosphere, ocean and wave wind stresses. Since τ_w is considered as a known source term, φ_w is assumed constant and known. φ_a and φ_o are unknown constants, aligned with the potentially distinct shear directions in either the atmosphere and ocean part of the SL. Using Equation 21 instead of wind stress conservation yields substituting Equation 13a with:

$$\left(u_{o,eff}^* \right)^2 e^{i\varphi_o} = (\lambda_u u_a^*)^2 e^{i\varphi_a} + |\tau_w| e^{i\varphi_w} / \rho_o \quad (22)$$

434 which is a two-fold constraint on both the norm and direction of the τ and $\tau_{o,eff}$. As a result, the closure equation for
 435 momentum is also bidimensional and set in C , which has an impact on the bulk closure and its algorithmic implemen-
 436 tation (see appendix C for more details).

437 Wind stresses τ obtained from bulk closures including τ_w are shown in Figs. 7 and 8 (red lines). All computations are
 438 done with $[[u]]_{z_0^1}^{z_a^1} = 11.5$ m/s, aligned with the i direction ($\text{Arg} = 0$). Figures 7 and 8 also feature τ_0 , the wind stress that
 439 would be obtained in the absence of external wave stress ($\tau_w = 0$), i.e. using the two-sided bulk closures discussed
 440 in Sec. 4.3 (black lines, same on all subfigures). With the parameters described above, $\tau_0 \approx 0.23$ N/m², aligned in the
 441 i -direction ($\text{Arg} \tau_0 = 0$). On Fig. 7, each subfigure corresponds to a different value for $|\tau_w|$ (green lines), and covers the
 442 interval $-\pi < \text{Arg} \tau_w \leq +\pi$; on the other hand, Fig. 8 represents τ depending on $|\tau_w|$ for a limited set of values for
 443 $\text{Arg} \tau_w$ (legend box).

444 A first effect, observed in Fig. 7 only, arises from comparing $\tau_{o,eff}$ (blue lines) and τ_0 (black lines), the stresses trans-
 445 mitted to the ocean with and without the external τ_w wave stress. Expectedly, including τ_w drastically impacts $\tau_{o,eff}$
 446 (blue lines) in both norm and direction. As $|\tau_w|$ increases, $\tau_{o,eff}$ is progressively deviated from τ_0 towards τ_w . This can
 447 be easily inferred from Equation 21: τ_w is an external ocean stress contribution, in addition to the wind-stress τ (red
 448 lines). For example, for $\text{Arg} \tau_w = \pi$ (wave stress opposite to shear): in Fig. 7c ($|\tau_w| \approx |\tau_0|$), the wind and wave stresses
 449 counterbalance each other, so that in $\tau_{o,eff}$ is nearly zero. In Fig. 7d ($|\tau_w| \approx 3|\tau_0|$), the wave stress dominates over
 450 the wind stress, and thus the resulting stress transmitted to the ocean can be contrary to the direction $[[u]]_{z_0^1}^{z_a^1}$. The
 451 wave-dominated stress balance represented in Fig. 7d is analogous to low-wind conditions, when the wind stress is
 452 small compared to the swell-induced one, hence the momentum flux can be transferred upward (from the ocean to
 453 the atmosphere, e.g. Jiang et al., 2016; Höglström et al., 2018), with negative drag transfer coefficient (Smedman et al.,
 454 1994). As previously mentioned, with our 2D framework derived from Equation 22, the effective drag coefficient is a
 455 complex number. Hence it can account for upward momentum transfer (when $\text{Arg} \left(\tau / [[u]]_{z_0^1}^{z_a^1} \right) \approx \pi$), but also any stress
 456 deflection due to a given external wave-induced stress τ_w , which can be fully independent from near-surface veloc-
 457 ities (e.g., in the presence of swell). Since classical bulk closures neglect the velocity profile evolution in the ONSL,
 458 they imply $C_D \in \mathbb{R}_+^*$, and thus can only transfer momentum in the direction of $[[u]]_0^{z_a^1}$ (resp. $u(z_a^1)$) for relative-winds
 459 (resp. absolute-winds) closures. In that regard, our ONSL-including formalism allows more flexibility for representing
 460 wave-induced deflections of the wind stress, as their mathematical structure allows $\text{Arg} \tau_{o,eff}$ to be decorrelated from
 461 $\text{Arg} [[u]]_{z_0^1}^{z_a^1}$.

462 A second effect, observed in both Figs. 7 and 8, arises from comparing τ (red lines) and τ_0 (black lines), the wind
 463 stresses with and without τ_w . This effect is less obvious, but it becomes more and more perceivable with increasing
 464 $|\tau_w|$: the presence of an external wave-induced stress also perturbrates τ , the wind stress resulting from the bulk
 465 closure. As Figs. 7c, 7d and 8a suggest, the impact becomes prevalent on $|\tau|$ with strong $|\tau_w|$ in opposite direction
 466 compared to $[[u]]_{z_0^1}^{z_a^1}$. However, Fig. 8b also shows that $\text{Arg} \tau$, the wind stress norm, is also lightly impacted. This can
 467 also be perceived upon careful examination of the red arrows in Figs. 7c and 7d. While the first effect described
 468 above is attributable to τ_w increasing the effective stress transmitted to the ocean, this second effect derives from
 469 the impact of τ_w on the τ closure itself. Indeed, by including τ_w , the stress exerted on the ONSL is enhanced by τ_w ; as
 470 a reaction to this, the ocean velocity dimensionless group is changed. Consequently, the bulk closure, which includes
 471 an integration of the velocity group in the ONSL (see Equation 10a), is altered. The turbulent closure adapts itself
 472 so that the resulting $u_{o,eff}^*$ (resp. u_a^*) properly connects $u(z_0^1)$ (resp. $u(z_a^1)$) at the bottom (resp. top) of the surface
 473 layer, with $\partial_z u$ being driven by $\tau + \tau_w$ (instead of τ) in the ONSL. As for the first effect, this second effect of τ_w on
 474 momentum closure cannot be represented by one-sided closure, since they do not integrate velocity dimensionless

475 groups on the ONSL.

476 Solution profiles arising from two-sided closures, with or without waves, are displayed on Fig. 9. The profiles without
 477 waves, or with effective diffusivities taking into account the Langmuir number Equation 20 are very close to each
 478 other, hence, the impact of Equation 20 is negligible in our framework, focusing on the ONSL. This does not mean that
 479 Equation 20 has a small impact on the whole ocean, as this parameterization is to be used on the whole OBL instead
 480 of, for example, a standard “K-profile” parameterization (Troen and Mahrt, 1986). Solution profiles with $\tau_{o,eff} = \tau + \tau_w$
 481 are also represented in colored dashed plots. Injecting τ_w has an impact in both the atmosphere and the ocean SL, with
 482 the changes being more prevalent in the ocean, as expected from Equation 21. In Fig. 9, the near-surface winds and
 483 currents are assumed aligned, hence $u_j(z) = 0$ for the waveless (black lines) and Langmuir profiles (dotted black). Closer
 484 inspection of the u_i profiles in the direct vicinity of the ocean surface (see Figs. 9c, 9i and 9o) illustrates the second
 485 effect described above on τ_w perturbing the turbulent closure. If τ_w is in the same direction as $[[u]]_{z_0^1}^{z_a^1}$ ($\text{Arg } \tau_w = 0$
 486 here), then including τ_w decreases u_a^* . Indeed, in that case, τ_w contributes jointly with τ to make $u(z_a^1)$ connect $u(z_0^1)$.
 487 Hence, u_a^* , which scales the shear-induced stress, is dampened, because the connection between $u(z_a^1)$ and $u(z_0^1)$ is
 488 also partly sustained by τ_w . On the contrary, if τ_w is opposing $[[u]]_{z_0^1}^{z_a^1}$ ($\text{Arg } \tau_w = \pi$ here), then including τ_w increases u_a^* :
 489 the shear-induced stress needs to be stronger to connect $u(z_0^1)$ with $u(z_a^1)$, because it also has to counteract τ_w in the
 490 ONSL. The intermediate cases in terms of direction ($\text{Arg } \tau_w = \pi/4, \pi/2, 3\pi/4$ here) cover the spectrum between both
 491 extreme cases presented above. In such intermediate cases, the solution profiles are deflected from the i -direction
 492 (hence $u_j \neq 0$), so that when the velocity groups are closed in the ONSL with $(\tau_w)_j \neq 0$, $u(z_0^1)$, which is aligned in the
 493 i -direction, is properly reached, and the j -component of τ_w is cancelled out.

494 The methods and results presented in this section attempt at representing wave impact while staying within the
 495 framework of MOST-derived bulk closure algorithms. It should however be reminded that since MOST does not hold
 496 in the presence of a significant WBL, an accurate and more legitimate representation of atmosphere - wind - ocean
 497 coupling cannot be formulated in this framework. Coupled wave boundary layer models are the designated tool for
 498 tackling this problem (see Chalikov and Rainchik, 2011, for a review).

499 | Radiative flux including ONSL parameterization

500 Radiative fluxes have been neglected from classical atmosphere-only bulk closures, since they are assumed indepen-
 501 dent of z in the lowest few meters of the atmosphere (see footnote 2 in Monin and Obukhov, 1954), and the radiative
 502 budget of the atmosphere SL is in equilibrium. Both these hypotheses are reasonably accurate in the context of
 503 atmosphere-only closures. However, in our two-sided framework, accounting for radiative fluxes (and thus lifting the
 504 ONSL-2) hypothesis) is required for two reasons. First, the radiative budget on the full SL is not in equilibrium: the
 505 net radiative flux at the air-sea interface is not zero (see Sect. 5.3.1). Second, shortwave radiative fluxes can display
 506 noticeable vertical gradients over the ONSL (see Sect. 5.3.2).

507 Let us call Q_{lw}^0 the net longwave flux at the ocean surface (i.e., accounting for surface blackbody radiation) and Q_{sw}^0 the
 508 net surface solar radiation (i.e., accounting for surface albedo), both fluxes being positive downwards. The boundary
 509 condition on θ at the ocean surface ($z = 0^-$) now reads:

$$510 \quad \mathcal{K}_{o,\theta}^{ad}(0^-) \partial_z \theta|_{z=0^-} = \frac{Q^H - Q_{lw}^0 - Q_{sw}^0}{\rho_o c_o^p} \quad (23)$$

where $\mathcal{K}_{\theta,\theta}^{ad}(z) = (\kappa u_o^*(-z) + \mathcal{K}_{\theta,\theta}^v) / \phi_o^h(-z/L_o)$ can be derived from Equation 10b. The minus sign in front of radiative fluxes is due to the z -axis being orientated upwards. It should also be mentioned that models typically do not inject Q_{sw}^0 as a boundary condition and instead prescribe it as an additional volumetric heat source term in the few first vertical levels (Jerlov, 1976). Since here we only focus on the SL, which is not treated by models, we will retain the shortwave-including form Equation 23. Theoretically, Q_{lw}^0 should be unknown since it includes an upward flux $(\theta(0))^4$ and only $\theta(z_o^1)$ is known. We will however assume Q_{lw}^0 to be known accurately enough, since $\theta(z=0) \approx 290$ K and previous results have shown that within our hypotheses, $|\theta(z=0) - \theta(z_o^1)| = O(1 \text{ K})$.

5.3.1 | Constant ONSL radiative flux approximation

As a first step, let us consider the simplified case where both radiative fluxes are deemed constant on the ONSL, i.e. Equation 23 is valid for $z_o^1 \leq z \leq 0$. In that case, the ONSL is still a constant flux layer, which can be described as an invariant group similar to Equation 10b. The right member of Equation 23 can thus be described as $u_o^* \theta_{o,rad}^{*,0}$ with a constant $\theta_{o,rad}^{*,0}$ scale to be determined. The presence of radiative fluxes in Equation 23 yields substituting Equation 13b with:

$$\theta_{o,rad}^{*,0} = \lambda_\theta \theta_a^* - \frac{Q_{lw}^0 + Q_{sw}^0}{\rho_o c_o^p \lambda_u u_a^*} \quad (24)$$

where the first term arises from sensible heat conservation through the ocean - atmosphere interface. Since here, Equation 23 is assumed true on $[z_o^1; 0]$, integrating it on this interval with Equation 24 injected leads to:

$$\llbracket \theta \rrbracket_{z_o^1}^{z_a^*} = \frac{\theta_a^*}{\kappa} \left[\ln \left(\frac{z_a^*}{z_{a,u}^r} \right) - \psi_a^h \left(\frac{z_a^*}{L_a} \right) \right] + \left(\frac{\lambda_\theta \theta_a^*}{\kappa} - \frac{Q_{lw}^0 + Q_{sw}^0}{\rho_o c_o^p \lambda_u u_a^*} \right) \left[\ln \left(\frac{-z_o^1}{\mu_m z_{a,u}^r / \lambda_u} \right) - \psi_o^h \left(\frac{-z_o^1}{L_o} \right) \right] \quad (25)$$

which is a radiation-including version of Equation 17b, in the idealized constant flux case, and can therefore be used jointly with Equation 17a as a bulk closure.

5.3.2 | Ocean surface layer with depth-varying solar flux

Longwave radiation is absorbed in (and emitted from) the first few millimeters of the ocean, hence we limit ourselves to directly injecting it as a boundary condition, and consider that it does not play a significant role on the dimensionless groups defined on $]z_o^1; 0[$. On the other hand, the shortwave (solar) flux can display perceivable gradients on the $[z_o^1; 0]$ interval, with $z_o^1 \approx -1$ m. In the upper ocean, its penetration can be parameterized as a combination of exponential modes depending on various factors such as incident angle and ocean biochemistry (e.g., Soloviev and Vershinsky, 1982; Morel and Antoine, 1994; Ohlmann and Siegel, 2000). Here we use a parameterization established by Paulson and Simpson (1981):

$$Q_{sw}(z) = Q_{sw}^0 \sum_{i=1}^9 A_i \exp(k_i z) \quad z_o^1 \leq z \leq 0 \quad (26)$$

539 where $k_i > 0$ [m⁻¹], $1 \leq i \leq 9$ characterize the typical damping depths, and A_i their relative intensities ($\sum A_i = 1$).
 540 Values of A_i and k_i can be extracted from Table 1 of Paulson and Simpson (1981). Including Equation 26 in the ONSL
 541 parameterization breaks the constant flux layer hypothesis (iONSL-1) and thus requires further adaptation of the bulk
 542 closure, compared to Sec. 5.3.1. Rendering depth-varying solar fluxes can be carried out by relaxing $\theta_{o,rad}^{*0}$ and letting
 543 it vary with z :

$$\theta_{o,rad}^*(z) = \lambda_\theta \theta_a^* - \frac{Q_{lw}^0 + Q_{sw}(z)}{\rho_o c_o^p \lambda_u u_a^*} \quad z_o^1 \leq z \leq 0 \quad (27)$$

544 In particular, $\theta_{o,rad}^*(z = 0^-) = \theta_{o,rad}^{*0}$. Integrating Equation 10b on $[z_o^1; 0]$ with θ_a^* substituted by $\theta_{o,rad}^{*0}$ from Equa-
 545 tion 27 (this can no longer be considered as an “invariant group”, since the flux depends on z), injecting Equation 26
 546 and rearranging terms yields the following two-sided closure on θ :

$$\begin{aligned} \llbracket \theta \rrbracket_{z_o^1}^{z_a^1} = & \frac{\theta_a^*}{\kappa} \left[\ln \left(\frac{z_a^1}{z_{a,u}^r} \right) - \psi_a^h \left(\frac{z_a^1}{L_a} \right) \right] + \left(\frac{\lambda_\theta \theta_a^*}{\kappa} - \frac{Q_{lw}^0}{\kappa \rho_o c_o^p \lambda_u u_a^*} \right) \left[\ln \left(\frac{-z_o^1}{\mu_m z_{a,u}^r / \lambda_u} \right) - \psi_o^h \left(\frac{-z_o^1}{L_o} \right) \right] \\ & - \frac{Q_{sw}^0}{\kappa \rho_o c_o^p \lambda_u u_a^*} \sum_{i=1}^9 A_i \left[e^{k_i z_{o,u}^r} \left(E_1(k_i z_{o,u}^r) - E_1(-k_i z_o^1) \right) - \int_0^{-z_o^1} \frac{\exp(-k_i L_o \zeta) (1 - \phi_o^h(\zeta))}{\zeta} d\zeta \right] \end{aligned} \quad (28)$$

549 where $z_{o,u}^r = \mu_m z_{a,u}^r / \lambda_u$, $e = \exp(1)$ and $E_1(x) = \int_x^\infty e^{-t} / t dt$ is the exponential integral with index 1. Expectedly,
 550 Equation 28 encompasses Equation 25; its last integral is a radiative-inclusive variant of the ψ_o^h integrated stability
 551 function, and cannot be determined analytically, in general. Since the radiative contributions of Equations 25 and 28
 552 are part of ONSL-specific terms of the closure, they can only be rendered by two-sided closures. Indeed, default
 553 classical closures (cool-skin including ones being a notable exception) neglect all processes potentially impacting $\partial_z \theta$
 554 in the ONSL, including radiation.

555 θ solution profiles arising from different bulk closures, including radiative-inclusive ones, are illustrated in Fig. 10. As
 556 expected, including radiative fluxes has an impact of the θ solution profiles. Under unstable stratification Figs. 10a
 557 suggest that during daytime (e.g. at $Q_{sw}^0 = 300$ W/m²), compared to radiation-neglecting bulks, the perceived
 558 surface temperature can be diminished by a few 0.1 K. This behavior is due to the bulk closure aiming at connecting
 559 the same $\theta(z_a^1)$ and $\theta(z_o^1)$ couple: if a positive radiative flux is enforced, then the bulk closure leads to a slightly colder
 560 surface temperature, to compensate for the additional heating in the ONSL, and still connect $\theta(z_o^1)$. It should be
 561 clear that in Fig. 10, $\theta(z_o^1)$ is taken as input, hence the results discussed only hold for the evolution of θ in the ONSL
 562 when $\llbracket \theta \rrbracket_{z_o^1}^{z_a^1}$ is known, and do not mean that the ocean surface is cooled down by incoming shortwave radiation. In non-
 563 stationary simulations, the solar flux would warm $\theta(z_o^1)$ through its impact on the θ boundary condition, and dominate
 564 over the relative cooling observed in Figs. 10a to 10c. At nighttime ($Q_{sw}^0 = 0$ W/m²), the total net radiation flux is
 565 negative since $Q_{lw}^0 < 0$, and the solution profiles are increasing with z (see Fig. 10c): the surface temperature is slightly
 566 warmer than $\theta(z_o^1)$, since the ONSL θ profile is dominated by a longwave-induced flux, cooling it down anew to $\theta(z_o^1)$.
 567 Under stable stratification, Figs. 10d to 10f suggest that similar conclusions hold, with θ profiles decreasing with z in
 568 the ONSL during daytime (see Fig. 10f), in contrast with shear-driven θ profile are then increasing with z . While the
 569 effects are expectedly more perceivable with constant fluxes than with fluxes progressively dampened with depth,
 570 the explanations given above hold in both cases.

6 | AN OFFLINE NUMERICAL ASSESSMENT OF TWO-SIDED CLOSURES

In both coupled or forced-ocean simulations, the implementation of two-sided SL parameterizations can swiftly be carried out by patching the existing bulk fixed-point algorithm to make it solve Equation 17 instead of Equation 3. Here we investigate the impact of our novelties by reassessing and comparing turbulent fluxes on offline computations, using ocean and atmosphere reanalyses as input data. For doing so, we compare fluxes obtained from global large-scale ocean and atmosphere reanalyses. The reference bulk formula is COARE 3.0 (Fairall et al., 2002) as per the `obulk` package (Brodeau et al., 2017). We perform standard absolute-winds, relative-winds and two-sided bulk closures for the year 2006, which has been close to the current era climatology. Ocean inputs are given by the ORYS2V4 dataset (Mercator Ocean, 2019), extracted at $z_o^1 \approx -0.5$ m, and atmosphere forcings are given by ERA-Interim (Dee et al., 2011), extracted from $z_a^1 = 10$ m. Since the two-sided bulk formula has only been introduced for the open ocean, all grid cells where the sea ice concentration exceeds 15% have been excluded from computations. While atmosphere moisture is included, in order to fit with our hypothesis, turbulent-scale moisture effects have been screened out by assuming $q(z=0) = q(z_a^1)$, thus resulting in null latent heat flux. Numerical results from these offline tests are shown in Figs. 11 and 12.

Fig. 11 shows the yearly mean discrepancy of turbulent fluxes when using two-sided bulk closures in comparison with standard relative-winds ones. A negative bias is observed on $|\tau|$, which was to be expected since including previously-neglected layers leads to velocity shear damping. The positive bias in Q^H is explained by the fact that on average, stratification is unstable, i.e., Q^H is “less negative” with two-sided closures than with standard ones. The larger mitigation values are reached where ocean currents are strong, in the Antarctic circumpolar current, the Kuroshio current and the Gulf stream. Fig. 12 shows 2006 daily time series of turbulent fluxes and surface fields at one location in the Kuroshio current ((149.25°E, 36.75°S), marked in Fig. 11). Fig. 12 suggests that punctually, turbulent flux mitigation from using two-sided closures can significantly alter the resulting fluxes. The biases between classical closures and two-sided ones are marked with a very high temporal variability, which was to be expected: our framework assumes that the ONSL directly responds to surface forcing from the atmosphere, hence the strong atmosphere variability is transferred into the upper layer of the ocean. Figure 12a suggests that while including relative winds yields stronger wind stress, using our two-sided lightly weakens it. This can be explained by the shear, which is typically less important in the two-sided framework, since across the ONSL, the currents will progressively adapt to the near-surface winds (see Fig. 12c). This observation is coherent with results presented in Sec. 5.1.

The impact on Q^H can be at times quite large, although it is negligible most of the year, for both relative-winds and two-sided closures (see Fig. 12b). On Fig. 11, sensible heat mitigation is relatively low at high latitudes because grid cells covered in sea ice have been screened out. As already pointed out in Sec. 4.1, the effects of our two-sided closures on the SST are negligible on average (in the order of 0.05 K). However, Fig. 12d features a few extreme events where two-sided closures significantly cool down the SST (early August, late September). These events are concomitant with low-wind conditions under unstable stratification, which is consistent with results already presented in Fig. 5b. The relatively weak reaction of SSTs can be explained by a combination of three factors. First, temperature (or equivalently, heat) mitigation is globally weaker than the velocity (stress) one since $\lambda_\theta \ll \lambda_u$. Second, this idealized test does not include radiative fluxes and their subsequent effects, which would generate stronger SST variability. Third, in this online test, the input temperature are not allowed to drift in time: only their instant reaction to SL parameterization is shown.

610 **7 | DISCUSSION**

611 We have introduced a formalism for extending air-sea turbulent flux parameterizations in order to make them account
612 for shear turbulence driven effects on both sides of the interface, including the ocean. Special care has been taken to
613 ensure by design the smoothness of solution profiles within the SL. The impact of our novelties in the SL treatment
614 has been investigated on both idealized and more realistic cases. In general, our findings affect near-surface velocity
615 profiles more than temperature ones. Occurrences with significant differences on turbulent air-sea flux determination
616 (up to 20%) have been underlined. The effects are mostly concentrated on the representation of surface velocity, which
617 in turn impacts the wind stress and sensible heat fluxes through their dependency on $z_{\alpha,u}^r$ and u_{α}^* . Such results may have
618 implications for describing debris transport in the upper ocean. Recent results on that field suggest strong variations in
619 the top meter of the ocean, albeit linearly varying with z (e.g. Laxague et al., 2018), instead of the logarithmic profiles
620 defined in Sec. 4. An interesting perspective would then be to build sturdier dimensionless groups for velocity profiles within
621 the ONSL to match the results found in such studies.

622 The main message of this paper is that typical bulk closures have not been designed for being directly used in forced-
623 ocean or coupled ocean-atmosphere settings, when ocean surface properties are unknown. One central inconsistency
624 we have lifted supporting this idea is that classical bulk closures do not depend on the ocean vertical discretization.
625 The two-sided formalism introduced above is adapted for using state-of-the-art bulk closures with nonzero depth
626 ocean information as input. We do admit relying on a crude surface layer representation and first neglecting physi-
627 cally determining phenomena, such as wave-induced enhanced momentum transfer or radiative penetration within
628 the ocean SL. Yet, classical bulk closures fully neglect this part of the ONSL, hence, they implicitly rely on even cruder
629 assumptions. Stripping down the SL parameterization to the simpler, mathematically more ergonomic formalism that
630 we have relied on was a necessary step for developing our framework. Moreover, historical bulk closures have first
631 been developed within a similarly idealized setting (i.e., shear-driven SL). Our approach is to propose a relevant frame-
632 work within which incorporating new parameterizations could be carried out, without altering the global consistency
633 of the SL scheme. Section 5 proposed a few examples of such extensions. We stand by the idea that explicitly pa-
634 rameterizing the ONSL, albeit in a crude way, is more legitimate than implicitly neglecting it. Indeed, since the ONSL
635 is usually assumed passive in classical closures, its impact of the surface physics is “hidden”. Consequently, we be-
636 lieve that explicitly acknowledging the ONSL, by formulating bulk closures including it, may attract attention towards
637 developing physically more realistic two-sided closures.

638 Four specific further development perspectives retain our attention. First, adapting our framework to two-sided
639 wave-permitting boundary layers effects on turbulent fluxes. Results obtained using simplified wave formulations are
640 briefly established and discussed in Sec. 5.2. However, our formalism cannot be used per se for representing the ocean
641 surface at the viscous sublayers under conditions of strong winds, where the problem geometry is changed and wave-
642 induced micro instabilities overshadow viscous stress. Accurately simulating fluxes under heterogeneous surfaces,
643 such as wave-deformed oceans, has been a considerable research challenge for decades, even from the broader
644 perspective of boundary layer meteorology (LeMone et al., 2019). Literature on this matter includes both simplified
645 models (Troitskaya and Rybushkina, 2008) and three-component ocean - wave - atmosphere coupling (Hristov et al.,
646 2003; Chen et al., 2007, 2013), which is well beyond the scope of this paper. Second, including moisture and salinity
647 influence on our two-sided algorithms ought to be carried out, since such effects are already present in one-sided
648 turbulent closures. This could be done by adapting the study of Bellenger et al. (2017), which proposes an extension
649 of the Zeng and Beljaars (2005) warm layer model for enhancing the representation of saline stratification in the upper

650 ocean layer. Third, the Equation 14 molecular constraint imposed at the $z = 0$ is a serious simplification compared
651 to the very rich physics of the viscous sublayers. In particular, the stress ratio at the interface has already been
652 investigated in the literature, with different values or dependencies underlined (Saunders, 1967; Robinson et al., 1984;
653 Ward and Donelan, 2006). Since no clear consensus has arisen from the aforementioned studies, Equation 14 has
654 been used as a minimal representation of surface constraint. However, our framework could swiftly incorporate
655 a more explicit parameterization by reformulating Equation 14 and integrating it within the two-sided closure. More
656 generally speaking, since our new formalism includes new physics, it also calls for calibrating anew bulk closures
657 (roughness and stability representations) from two-sided turbulent measurements. This could potentially limit the
658 spread between observations and parameterizations. Fourth, our study assumes that the ONSL immediately responds
659 to above-surface fast changes, which is usually not the case as the ocean kinematic viscosity is ≈ 30 times greater
660 than the atmosphere's. Soloviev et al. (2001) suggests rendering the nonstationarity of the ONSL by using a gradient
661 Richardson number and linking it to the Obukhov length. Such an endeavor is beyond the scope of the current paper,
662 where the stationarity of the ONSL is used as a working hypothesis.

663 On the longer-term perspective, we believe that parameterizing the SL in full at a continuous level clarifies the math-
664 ematical nature of the boundary conditions enforced between the ocean and the atmosphere. Due to their explicit
665 form (see Equation 1), classical air-sea boundary conditions are subject to being erroneously assimilated to Neumann
666 conditions. We however argue that the turbulent air-sea boundary conditions are, at the continuous level, equivalent
667 to a combination of Dirichlet and Neumann boundary conditions. If we consider that the surface layer solution pro-
668 files obtained from the parameterization scheme are correct, then imposing Equation 1 is mathematically equivalent
669 to imposing the continuity of the solutions and a constraint on their gradients at $z = 0$. In our opinion, transcribing
670 the air-sea coupling problem into such a simpler yet sturdier mathematical formalism would ease the further theoret-
671 ical development of turbulence-including coupling algorithms. At the practical, discrete level, connecting the surface
672 layer with computational domains could be implemented by using specifically designed splines built from the chosen
673 parameterization set.

674 Acknowledgements

675 This work was supported by the French national research agency through the ANR project "COCOA" (COmprehensive
676 Coupling approach for the Ocean and the Atmosphere), grant ANR-16-CE01-0007. We would like to express our
677 gratitude to Deborah Verfaillie for her careful proofreading, and to Bablu Sinha for editing this article. All authors
678 would like to warmly thank both anonymous reviewers who provided elaborated and insightful comments which
679 showed that the manuscript had been examined with care and substantially improved it.

680 Conflict of interest

681 The authors declare that they have no conflict of interest.

682 A | ANALYTICAL DETAILS ON THE NEW ASL DIMENSIONLESS GROUP

683 A.1 | Exact ASL integrations using the Högström (1988) stability functions

684 Here we integrate u from Equation 5a downwards from z_a^1 to $z \in [0; z_a^1[$, without any prior assumption on $\mathcal{K}_{a,u}^{\mathcal{V}}$ and
685 using ϕ_a^m as described by Högström (1988):

$$686 \quad \phi_a^m(\zeta) = 1 + 5\zeta \quad \text{if } \zeta \geq 0 \quad (29a)$$

$$687 \quad \phi_a^m(\zeta) = (1 - 16\zeta)^{-1/4} \quad \text{if } \zeta < 0 \quad (29b)$$

688 Details on integrating θ from Equation 5b with ϕ_a^h from Högström (1988) are not given since the procedure is very
689 similar to that described below. In the stable case ($L_a, \zeta \geq 0$), integrating Equation 5a with Equation 29a injected and
690 rearranging terms leads to:

$$691 \quad u(z_a^1) - u(z) = \frac{(u_a^*)^2}{L_a} \int_z^{z_a^1} \frac{(L_a + 5z')}{\kappa u_a^* z' + \mathcal{K}_{a,u}^{\mathcal{V}}} dz' \quad (30)$$

692 which directly yields:

$$693 \quad u(z_a^1) - u(z) = \frac{u_a^*}{\kappa} \left[\left(1 - \frac{5\mathcal{K}_{a,u}^{\mathcal{V}}}{\kappa u_a^* L_a} \right) \ln \left(\frac{z_a^1 + \mathcal{K}_{a,u}^{\mathcal{V}} / (\kappa u_a^*)}{z + \mathcal{K}_{a,u}^{\mathcal{V}} / (\kappa u_a^*)} \right) + \frac{5(z_a^1 - z)}{L_a} \right] \quad (31)$$

694 Doing a zeroth-order approximation of Equation 31 in the $\mathcal{K}_{a,u}^{\mathcal{V}} / (\kappa u_a^*) \ll z_a^1, |L_a|$ limit yields a form compatible with
695 Equation 7. In the unstable case ($L_a, \zeta < 0$), integrating Equation 5a with Equation 29b injected and using the $z' \leftrightarrow$
696 $\eta = (1 - 16\frac{z'}{L_a})^{1/4}$ change of variable yields:

$$697 \quad u(z_a^1) - u(z) = \frac{4u_a^*}{\kappa} \int_{\eta(z)}^{\eta(z_a^1)} \frac{\eta^2}{\eta^4 - 1 + \mathcal{K}_{a,u}^{\mathcal{V}} / \nu_0} d\eta \quad (32)$$

698 where $\nu_0 = -\kappa u_a^* L_a / 16 > 0$. Depending on the sign of $\xi = 1 - \mathcal{K}_{a,u}^{\mathcal{V}} / \nu_0$, integrating Equation 32 yields:

$$699 \quad u(z_a^1) - u(z) = \begin{cases} \frac{u_a^*}{\xi^{1/4} \kappa} \left[2\text{Arctan}(\eta \xi^{-1/4}) + \ln \left(\frac{\eta - \xi^{1/4}}{\eta + \xi^{1/4}} \right) \right]_{\eta=\eta(z)}^{\eta(z_a^1)}, & \text{if } \xi > 0 \\ \frac{4u_a^*}{\kappa} \left[(\eta(z))^{-1} - (\eta(z_a^1))^{-1} \right], & \text{if } \xi = 0, \\ \frac{\sqrt{2}u_a^*}{2(-\xi)^{1/4} \kappa} \left[2\text{Arctan} \left(\frac{\sqrt{2}(2\eta + \sqrt{2}(-\xi)^{1/4})}{2(-\xi)^{1/4}} \right) + 2\text{Arctan} \left(\frac{\sqrt{2}(2\eta - \sqrt{2}(-\xi)^{1/4})}{2(-\xi)^{1/4}} \right) \right. \\ \left. - \log \left(\eta^2 + \sqrt{2}(-\xi)^{1/4} \eta + \sqrt{-\xi} \right) + \log \left(\eta^2 - \sqrt{2}(-\xi)^{1/4} \eta + \sqrt{-\xi} \right) \right]_{\eta=\eta(z)}^{\eta(z_a^1)}, & \text{if } \xi < 0 \end{cases} \quad (33)$$

700 Injecting $\mathcal{K}_{a,u}^{\mathcal{V}} / (\kappa u_a^*) \ll z_a^1, |L_a|$ in Equation 33 yields $\xi \approx 1$, and thus only the $\xi > 0$ case of Equation 33 is relevant.
701 Assessing it at $z = 0$ yields:

$$702 \quad u(z_a^1) - u(0) = \frac{u_a^*}{\kappa} \left[2\text{Arctan}(\eta(z_a^1)) - \frac{\pi}{2} + \ln \left(\frac{\eta(z_a^1) - 1}{\eta(z_a^1) + 1} \right) - \ln \left(\frac{1 - \xi^{1/4}}{2} \right) \right] \quad (34)$$

703 A.2 | Asymptotic development on the molecular effect including ASL closure

704 In this section, we prove that integrating Equation 5 in the $\mathcal{K}_{a,u}^v, \mathcal{K}_{a,\theta}^v \ll \kappa u_a^* z_a^1, \kappa u_a^* |L_a|$ limit leads to Equation 7.
 705 For doing so, we go back to the ϕ_a^m, ϕ_a^h stability functions being generic, and assume that they satisfy the following
 706 constraints:

707 (h1) ϕ_a^m, ϕ_a^h are smooth over \mathbb{R} (i.e., they are continuous);

708 (h2) $\zeta \mapsto (1 - \phi_a^x(\zeta))/\zeta$ is integrable on $[0; z_a^1]$.

709 We assume that both these constraints are satisfied by most classical stability functions. Integrating either subequations of
 710 Equation 5 leads to:

$$711 \quad x(z_a^1) - x(z) = \frac{x_a^*}{\kappa} \int_{z'=z}^{z_a^1} \frac{\phi_a^x(z'/L_a)}{z' + x_a^v/(\kappa u_a^*)} dz' \quad (35)$$

712 where $x \in \{u, \theta\}$ and $x_a^v \in \{\mathcal{K}_{a,u}^v, \mathcal{K}_{a,\theta}^v\}$, chosen accordingly. Performing the change of variable $z' \mapsto \bar{z} = z + x_a^v/(\kappa u_a^*)$
 713 and rearranging terms in Equation 35 leads to:

$$714 \quad x(z_a^1) - x(z) = \frac{x_a^*}{\kappa} \left[\ln \left(\frac{z_a^1 + x_a^v/(\kappa u_a^*)}{z + x_a^v/(\kappa u_a^*)} \right) - \int_{\bar{z}=z+x_a^v/(\kappa u_a^*)}^{z_a^1+x_a^v/(\kappa u_a^*)} \frac{1 - \phi_a^x(\bar{z} - x_a^v/(\kappa u_a^*))}{\bar{z}} d\bar{z} \right] \quad (36)$$

715 Since $x_a^v \ll \kappa u_a^* z_a^1$, the numerator in the logarithm of Equation 36 can be reduced to z_a^1 . For the second, stability-
 716 considering term of Equation 36, we argue that it is equivalent to $-\psi_a^x(z_a^1) + \psi_a^x(z)$. Indeed:

717 if $z \lesssim z_a^1$, then $\bar{z} \approx z$. Since (h1) states that ϕ_a^x is smooth, the second term in Equation 36 is close to $-\psi_a^x(z_a^1) + \psi_a^x(z)$.

718 • If $z \ll z_a^1, |L_a|$, then $\bar{z} - x_a^v/(\kappa u_a^*) \ll 1$, and (h2) guarantees that the lower integration boundary can be approximated
 719 as $z = 0$;

720 B | ADAPTING TWO-SIDED BULK CLOSURES TO TURBULENT FLUX MEASUREMENTS CALIBRATED WITH NONZERO DEPTH OCEAN FIELDS

722 In Sec. 3, an estimate of $\mathcal{K}_{a,x}^v$ directly deduced from $z_{a,x}^r$ has been given (see Equation 9). This corresponds to our under-
 723 standing of the roughness heights in classical bulk closures, which match the heights at which MOST-derived solution
 724 profiles reach their expected "surface values". As a consequence, the adapted atmosphere bulk closure evaluated from
 725 the velocity and temperature jumps between $z = 0$ and z_a^1 are equivalent to classical bulk closures. However, ocean
 726 surface properties cannot be measured: only near-surface properties can, at a depth of a few millimeters (Donlon et al.,
 727 2002) at least. Below $\mathcal{K}_{a,x}^v, x \in \{u, \theta\}$ are evaluated anew so that the resulting two-sided bulk closure matches the ve-
 728 locity and temperature jumps from an arbitrary reference depth $z_o^{ms} \approx -1$ mm to z_a^1 . As a consequence, the computed
 729 fluxes will match the experimental setting measurements $z_{a,u}^r$ and $z_{a,\theta}^r$ have actually been tuned for. The method
 730 described below can also be generalized for cases in which the reference currents and temperatures measurement
 731 depths are distinct.

Integrating Equation 10 on $[z_o^{ms}; 0]$, with Equations 13 and 15 injected, leads to, for $x \in \{u, \theta\}$:

$$\llbracket x \rrbracket_{z_o^{ms}}^0 = \frac{\lambda_x x_a^*}{\kappa} \ln \left(\frac{-z_o^{ms} + \mu_m \mathcal{K}_{a,x}^V / (\lambda_u \kappa u_a^*)}{\mu_m \mathcal{K}_{a,x}^V / (\lambda_u \kappa u_a^*)} \right) \quad (37)$$

where stratification has been neglected, since $|z_o^{ms}| \approx 1 \text{ mm} \ll |L_o|$. Summing Equations 8 and 37, rearranging terms, and identifying the resulting denominator to $z_{a,x}^r$, yields, for $x \in \{u, \theta\}$:

$$\frac{\mathcal{K}_{a,x}^V}{\kappa u_a^*} \left(\frac{-z_o^{ms} + \mu_m \mathcal{K}_{a,x}^V / (\lambda_u \kappa u_a^*)}{\mu_m \mathcal{K}_{a,x}^V / (\lambda_u \kappa u_a^*)} \right)^{-\lambda_x} = z_{a,x}^r \quad (38)$$

which is a condition for two-sided bulk closures to match classical bulk closures, assuming they have been tuned from ocean measurements at $z = z_o^{ms}$. In other words, evaluating $z_{a,x}^r$ from a given classical bulk formula, and then solving Equation 38 on $\mathcal{K}_{a,x}^V$, leads to two-sided bulk closures being consistent with solution jumps from z_o^{ms} to z_a^1 . In general, determining $\mathcal{K}_{a,x}^V$ from $z_{a,x}^r$ through Equation 38 can only be done numerically. However, a more exploitable form can be obtained by assuming $|z_o^{ms}| \gg \mu_m \mathcal{K}_{a,x}^V / (\lambda_u \kappa u_a^*)$, i.e., that the reference ocean measurement depth is large compared to the ocean roughness depth. Figs. 3c and 3f suggest that such an assumption is reasonable. As a result, Equation 38 can be simplified to:

$$\mathcal{K}_{a,x}^V \approx \kappa u_a^* \left[z_{a,x}^r \left(\frac{-z_o^{ms} \lambda_u}{\mu_m} \right)^{\lambda_x} \right]^{\frac{1}{1+\lambda_x}} \quad (39)$$

WAVE-FORCED ADAPTED BULK ALGORITHMS

Equation 22 yields substituting Equation 17a with:

$$\llbracket u \rrbracket_{z_o^1}^{z_a^1} = \frac{u_a^* e^{i\varphi_a}}{\kappa} \mathcal{G}_a(\mathbf{x}_a^*) + \frac{u_{o,eff}^* e^{i\varphi_o}}{\kappa} \mathcal{G}_o(\mathbf{x}_o^*) \quad (40)$$

where:

$$\mathcal{G}_a(\mathbf{x}_a^*) = \ln \left(\frac{z_a^1}{z_{a,u}^r} \right) - \psi_a^m \left(\frac{z_a^1}{L_a} \right) \quad (41a)$$

$$\mathcal{G}_o(\mathbf{x}_o^*) = \ln \left(\frac{-z_o^1}{z_{u,o}^r} \right) - \psi_o^m \left(\frac{-z_o^1}{L_o} \right) \quad (41b)$$

A slight adaptation of fixed-point bulk algorithms is needed in order to make them solve Equation 40 instead of Equation 17a. Indeed, non-wave including bulk algorithms rely on iterating over u_a^* with the following procedure:

$$u_a^{*,\{k+1\}} = \frac{\kappa \left| \llbracket u \rrbracket_{z_o^1}^{z_a^1} \right|}{\mathcal{G}_a(\mathbf{x}_a^{*,\{k\}}) + \lambda_u \mathcal{G}_o(\mathbf{x}_{o,eff}^{*,\{k\}})} \quad (42)$$

754 where $k \in \mathbb{N}$ denotes bulk algorithm iterations. Solving Equation 40 can no longer be done by simply injecting Equa-
 755 tion 42 as in the presence of τ_w , $u_{o,eff}^*$ is not proportional to u_a^* anymore. Instead, we propose the following four-step
 756 procedure, deduced from Equations 22 and 40:

$$757 \quad u_a^{*,\{k+1\}} = \frac{1}{\mathcal{G}_a(\mathbf{x}_a^{*,\{k\}})} \left| \kappa \llbracket u \rrbracket_{z_0^1}^{z_a^1} - u_o^{*,\{k\}} \mathcal{G}_o(\mathbf{x}_{o,eff}^{*,\{k\}}) e^{i\varphi_o^{\{k\}}} \right| \quad (43a)$$

$$758 \quad \varphi_a^{\{k+1\}} = \text{Arg} \left\{ \kappa \llbracket u \rrbracket_{z_0^1}^{z_a^1} - u_o^{*,\{k\}} \mathcal{G}_o(\mathbf{x}_{o,eff}^{*,\{k\}}) e^{i\varphi_o^{\{k\}}} \right\} \quad (43b)$$

$$759 \quad u_{o,eff}^{*,\{k+1\}} = \sqrt{\left(\lambda_u u_a^{*,\{k+1\}} \right)^2 e^{i\varphi_a^{\{k+1\}}} + \frac{|\tau_w|}{\rho_o} e^{i\varphi_w}} \quad (43c)$$

$$7 \quad \varphi_o^{\{k+1\}} = \text{Arg} \left\{ \left(\lambda_u u_a^{*,\{k+1\}} \right)^2 e^{i\varphi_a^{\{k+1\}}} + \frac{|\tau_w|}{\rho_o} e^{i\varphi_w} \right\} \quad (43d)$$

751 where $\mathcal{G}_a > 0$ is implicitly assumed, which is reasonable since $|z_\alpha^1| \gg |z_{\alpha,u}^1|$ and $\psi_a^m \leq 1$ over the ocean.

762 references

- 763 Bellenger, H., Drushka, K., Asher, W., Reverdin, G., Katsumata, M. and Watanabe, M. (2017) Extension of the prognostic model
 764 of sea surface temperature to rain-induced cool and fresh lenses. *J. Geophys. Res. Oc.*, **122**, 484–507.
- 765 Bressan, A. and Constantin, A. (2019) The deflection angle of surface ocean currents from the wind direction. *J. Geophys. Res.*
 766 *Oc.*, **124**, 7412–7420.
- 767 Brodeau, L., Barnier, B., Gulev, S. K. and Woods, C. (2017) Climatologically significant effects of some approximations in the
 768 bulk parameterizations of turbulent air–sea fluxes. *J. Phys. Oceanogr.*, **47**, 5–28.
- 769 Buckingham, E. (1914) On physically similar systems; Illustrations of the use of dimensional equations. *Phys. Rev.*, **4**, 345.
- 770 Businger, J. A., Wyngaard, J. C., Izumi, Y. and Bradley, E. F. (1971) Flux-profile relationships in the atmospheric surface layer.
 771 *J. Atmos. Sci.*, **28**, 181–189.
- 772 Golik, D. and Rainchik, S. (2011) Coupled numerical modelling of wind and waves and the theory of the wave boundary
 773 layer. *Bound.-Layer Meteorol.*, **138**, 1–41.
- 774 Chen, S., Qiao, F., Huang, C. J. and Zhao, B. (2018) Deviation of wind stress from wind direction under low wind conditions.
 775 *J. Geophys. Res. Oc.*, **123**, 9357–9368.
- 776 Chen, S. S., Price, J. F., Zhao, W., Donelan, M. A. and Walsh, E. J. (2007) The CBLAST-Hurricane program and the next-
 777 generation fully coupled atmosphere–wave–ocean models for hurricane research and prediction. *Bull. Am. Meteorol. Soc.*,
 778 **88**, 311–318.
- 779 Chen, S. S., Zhao, W., Donelan, M. A. and Tolman, H. L. (2013) Directional wind–wave coupling in fully coupled atmo-
 780 sphere–wave–ocean models: Results from CBLAST-Hurricane. *J. Atmos. Sci.*, **70**, 3198–3215.
- 781 Churchill, J. H. and Csanady, G. T. (1983) Near-surface measurements of quasi-lagrangian velocities in open water. *J. Phys.*
 782 *Oceanogr.*, **13**, 1669–1680.
- 783 Csanady, G. T. (1984) The free surface turbulent shear layer. *J. Phys. Oceanogr.*, **14**, 402–411.
- 784 Dawe, J. T. and Thompson, L. (2006) Effect of ocean surface currents on wind stress, heat flux, and wind power input to the
 785 ocean. *Geophys. Res. Lett.*, **33**.

- 786 Dee, D., Uppala, S., Simmons, A., Berrisford, P., Poli, P., Kobayashi, S., Andrae, U., Balmaseda, M., Balsamo, G., Bauer, P. et al.
787 (2011) The ERA-Interim reanalysis: Configuration and performance of the data assimilation system. *Quart. J. Roy. Meteorol.*
788 *Soc.*, **137**, 553–597.
- 789 Donelan, M. A. (1982) The dependence of the aerodynamic drag coefficient on wave parameters. In *Proc. First Int. Conf. on*
790 *Meteorol. and Air-Sea Interaction of the Coastal Zone*, 381–387.
- 791 Donlon, C. J., Minnett, P. J., Gentemann, C., Nightingale, T. J., Barton, I. J., Ward, B. and Murray, M. J. (2002) Toward improved
validation of satellite sea surface skin temperature measurements for climate research. *J. Clim.*, **15**, 353–369.
- 792 Drennan, W. M., Graber, H. C., Hauser, D. and Quentin, C. (2003) On the wave age dependence of wind stress over pure wind
793 seas. *J. Geophys. Res. Oc.*, **108**.
- 794 Frulle, B., Laval, J.-P., Sullivan, P. P. and Werne, J. (2002) A new dynamical subgrid model for the planetary surface layer.
795 Part I: The model and a priori tests. *J. Atmos. Sci.*, **59**, 861–876.
- 797 Duhaut, T. H. A. and Straub, D. N. (2006) Wind stress dependence on ocean surface velocity: Implications for mechanical
798 energy input to ocean circulation. *J. Phys. Oceanogr.*, **36**, 202–211.
- 799 Emanuel, K. A. (1986) An air-sea interaction theory for tropical cyclones. Part I: Steady-state maintenance. *J. Atmos. Sci.*, **43**,
800 585–605.
- 801 Esters, L., Breivik, Ø., Landwehr, S., ten Doeschate, A., Sutherland, G., Christensen, K. H., Bidlot, J.-R. and Ward, B. (2018)
802 Turbulence scaling comparisons in the ocean surface boundary layer. *J. Geophys. Res. Oc.*, **123**, 2172–2191.
- 803 Fairall, C., Bradley, E. F., Godfrey, J., Wick, G., Edson, J. B. and Young, G. (1996) Cool-skin and warm-layer effects on sea
804 surface temperature. *J. Geophys. Res. Oc.*, **101**, 1295–1308.
- 805 Fairall, C. W., Bradley, E. F., Hare, J. E., Grachev, A. A. and Edson, J. B. (2002) Bulk parametrization of air-sea fluxes: Updates
806 and verification for the COARE algorithm. *J. Clim.*, 571–591.
- 807 Geernaert, G. L. (1988) Measurements of the angle between the wind vector and wind stress vector in the surface layer over
808 the North Sea. *J. Geophys. Res. Oc.*, **93**, 8215–8220.
- 809 Geernaert, G. L., Hansen, F., Courtney, M. and Herbers, T. (1993) Directional attributes of the ocean surface wind stress vector.
810 *J. Geophys. Res. Oc.*, **98**, 16571–16582.
- 811 Geernaert, G. L., Larsen, S. E. and Hansen, F. (1987) Measurements of the wind stress, heat flux, and turbulence intensity
812 during storm conditions over the north sea. *J. Geophys. Res. Oc.*, **92**, 13127–13139.
- 813 Grachev, A. A., Fairall, C. W., Hare, J. E., Edson, J. B. and Miller, S. D. (2003) Wind stress vector over ocean waves. *J. Phys.*
814 *Oceanogr.*, **33**, 2408–2429.
- 815 Halpern, D. and Reed, R. K. (1976) Heat budget of the upper ocean under light winds. *J. Phys. Oceanogr.*, **6**, 972–975.
- 816 Höglström, U. (1988) Non-dimensional wind and temperature profiles in the atmospheric surface layer: A re-evaluation.
817 *Bound.-Layer Meteorol.*, **42**, 55–78.
- 818 Höglström, U., Sahlée, E., Smedman, A.-S., Rutgersson, A., Nilsson, E., Kahma, K. K. and Drennan, W. M. (2018) The transition
819 from downward to upward air-sea momentum flux in swell-dominated light wind conditions. *J. Atmos. Sci.*, **75**, 2579–
820 2588.
- 821 Hristov, T., Miller, S. and Friehe, C. (2003) Dynamical coupling of wind and ocean waves through wave-induced air flow. *Nature*,
822 **422**, 55.
- 823 Jerlov, N. G. (1976) *Marine optics*. Elsevier.

- 824 Jiang, Q., Sullivan, P., Wang, S., Doyle, J. and Vincent, L. (2016) Impact of swell on air–sea momentum flux and marine boundary
825 layer under low-wind conditions. *J. Atmos. Sci.*, **73**, 2683–2697.
- 826 Johnson, H. K., Højstrup, J., Vested, H. J. and Larsen, S. E. (1998) On the dependence of sea surface roughness on wind waves.
827 *J. Phys. Oceanogr.*, **28**, 1702–1716.
- 828 Kelly, K. A., Dickinson, S., McPhaden, M. J. and Johnson, G. C. (2001) Ocean currents evident in satellite wind data. *Geophys.*
829 *Res. Lett.*, **28**, 2469–2472.
- 830 Kent, E. C., Kennedy, J. J., Smith, T. M., Hirahara, S., Huang, B., Kaplan, A., Parker, D. E., Atkinson, C. P., Berry, D. I., Carella,
831 G., Fukuda, Y., Ishii, M., Jones, P. D., Lindgren, F., Merchant, C. J., Morak-Bozzo, S., Rayner, N. A., Venema, V., Yasui, S. and
832 Zhang, H.-M. (2017) A call for new approaches to quantifying biases in observations of sea surface temperature. *Bull. Am.*
833 *Meteorol. Soc.*, **98**, 1601–1616.
- 834 Kitaigorodskii, S. A. (1965) On the roughness parameter of the sea surface and the calculation of momentum flux in the near
surface layer of the atmosphere. *Izv., Atmos. Oceanic Phys.*, **1**, 973–988.
- 835 Large, W. B. (2006) Surface fluxes for practitioners of global ocean data assimilation. In *Ocean Weather Forecasting. An Inte-*
836 *grated View of Oceanography* (eds. E. P. Chassignet and J. Verron), chap. 9, 229–270. Springer.
- 837 Large, W. G. (1998) Modeling and parameterizing ocean planetary boundary layers. In *Ocean Modeling and Parameterization*
838 (eds. E. P. Chassignet and J. Verron), vol. 516, chap. 3, 81–120. Springer.
- 839 Large, W. G., Patton, E. G., DuVivier, A. K., Sullivan, P. P. and Romero, L. (2019) Similarity theory in the surface layer of large-
840 eddy simulations of the wind-, wave-, and buoyancy-forced Southern Ocean. *J. Phys. Oceanogr.*, **49**, 2165–2187.
- 841 Lavague, N. J. M., Özgökmen, T. M., Haus, B. K., Novelli, G., Shcherbina, A., Sutherland, P., Guigand, C. M., Lund, B., Mehta,
842 S., Alday, M. and Molemaker, J. (2018) Observations of near-surface current shear help describe oceanic oil and plastic
843 transport. *Geophys. Res. Lett.*, **45**, 245–249.
- 844 LeMone, M. A., Angevine, W. M., Bretherton, C. S., Chen, F., Dudhia, J., Fedorovich, E., Katsaros, K. B., Lenschow, D. H., Mahrt,
845 L., Patton, E. G., Sun, J., Tjernström, M. and Weil, J. (2019) 100 years of progress in boundary layer meteorology. *Meteorol.*
846 *Monogr.*, **59**, 9.1–9.85.
- 847 Li, Q., Reichl, B. G., Fox-Kemper, B., Adcroft, A. J., Belcher, S. E., Danabasoglu, G., Grant, A. L. M., Griffies, S. M., Hallberg, R.,
848 Hara, T., Harcourt, R. R., Kukulka, T., Large, W. G., McWilliams, J. C., Pearson, B., Sullivan, P. P., Van Roekel, L., Wang, P.
849 and Zheng, Z. (2019) Comparing ocean surface boundary vertical mixing schemes including Langmuir turbulence. *J. Adv.*
850 *Model. Earth Syst.*, **11**, 3545–3592.
- 851 Louis, J.-F. (1979) A parametric model of vertical eddy fluxes in the atmosphere. *Boundary-Layer Meteorol.*, **17**, 187–202.
- 852 Mcleish, W. and Putland, G. E. (1975) Measurements of wind-driven flow profiles in the top millimeter of water. *J. Phys.*
853 *Oceanogr.*, **5**, 516–518.
- 854 McWilliams, J. C. and Sullivan, P. P. (2000) Vertical mixing by Langmuir circulations. *Spill Sci. Technol. Bull.*, **6**, 225–237.
- 855 McWilliams, J. C., Sullivan, P. P. and Moeng, C.-H. (1997) Langmuir turbulence in the ocean. *J. Fluid Mech.*, **334**, 1–30.
- 856 Mercator Ocean (2019) Glorys2v4. Data retrieved from Copernicus: <http://marine.copernicus.eu/>.
- 857 Monin, A. S. and Obukhov, A. M. (1954) Basic laws of turbulent mixing in the surface layer of the atmosphere. *Trudy Akad.*
858 *Nauk SSSR Geof. Inst.*, **24**, 163–187.
- 859 Morel, A. and Antoine, D. (1994) Heating rate within the upper ocean in relation to its bio–optical state. *J. Phys. Oceanogr.*,
860 **24**, 1652–1665.

- 862 Neelin, J. D., Latif, M., Allaart, M. A. F., Cane, M. A., Cubasch, U., Gates, W. L., Gent, P. R., Ghil, M., Gordon, C., Lau, N. C.,
863 Mechoso, C. R., Meehl, G. A., Oberhuber, J. M., Philander, S. G. H., Schopf, P. S., Sperber, K. R., Sterl, K. R., Tokioka, T.,
864 Tribbia, J. and Zebiak, S. E. (1992) Tropical air-sea interaction in general circulation models. *Clim. Dyn.*, **7**, 73–104.
- 865 Obukhov, A. (1971) Turbulence in an atmosphere with a non-uniform temperature. *Bound.-Layer Meteorol.*, **2**, 7–29.
- 866 Ohmann, J. C. and Siegel, D. A. (2000) Ocean radiant heating. Part II: Parameterizing solar radiation transmission through the
867 upper ocean. *J. Phys. Oceanogr.*, **30**, 1849–1865.
- 868 Oost, W., Komen, G., Jacobs, C. and Van Oort, C. (2002) New evidence for a relation between wind stress and wave age from
8 measurements during ASGAMAGE. *Bound.-Layer Meteorol.*, **103**, 409–438.
- 870 Pacanowski, R. C. (1987) Effect of equatorial currents on surface stress. *J. Phys. Oceanogr.*, **17**, 833–838.
- 871 Patton, E. G., Sullivan, P. P., Kosović, B., Dudhia, J., Mahrt, L., Žagar, M. and Marić, T. (2019) On the influence of swell propa-
872 gation angle on surface drag. *J. Appl. Meteor. Climatol.*, **58**, 1039–1059.
- 873 Paulson, C. A. (1970) The mathematical representation of wind speed and temperature profiles in the unstable atmospheric
874 surface layer. *J. Appl. Meteorol.*, **9**, 857–861.
- 875 Paulson, C. A. and Simpson, J. J. (1981) The temperature difference across the cool skin of the ocean. *J. Geophys. Res. Oc.*, **86**,
876 11044–11054.
- 877 Renault, L., Lemarié, F. and Arsouze, T. (2019a) On the implementation and consequences of the oceanic currents feedback
878 in ocean–atmosphere coupled models. *Ocean Model.*, **141**, 101423.
- 879 Renault, L., Marchesiello, P., Masson, S. and McWilliams, J. C. (2019b) Remarkable control of western boundary currents by
880 eddy killing, a mechanical air–sea coupling process. *Geophys. Res. Lett.*, **46**, 2743–2751.
- 881 Renault, L., Molemaker, M. J., McWilliams, J. C., Shchepetkin, A. F., Lemarié, F., Chelton, D., Illig, S. and Hall, A. (2016) Modu-
882 lation of wind work by oceanic current interaction with the atmosphere. *J. Phys. Oceanogr.*, **46**, 1685–1704.
- 883 Robinson, I. S., Wells, N. C. and Charnock, H. (1984) The sea surface thermal boundary layer and its relevance to the measure-
884 ment of sea surface temperature by airborne and spaceborne radiometers. *Int. J. Remote Sens.*, **5**, 19–45.
- 885 Saunders, P. M. (1967) The temperature at the ocean–air interface. *J. Atmos. Sci.*, **24**, 269–273.
- 886 Sandman, A.-S., Tjernström, M. and Högström, U. (1994) The near-neutral marine atmospheric boundary layer with no surface
887 shearing stress: A case study. *J. Atmos. Sci.*, **51**, 3399–3411.
- 888 Smith, S. D. (1988) Coefficients for sea surface wind stress, heat flux, and wind profiles as a function of wind speed and
889 temperature. *J. Geophys. Res. Oc.*, **93**, 15467–15472.
- 890 Smyth, W. D., Skyllingstad, E. D., Crawford, G. B. and Wijesekera, H. (2002) Nonlocal fluxes and Stokes drift effects in the
891 K-profile parameterization. *Oc. Dyn.*, **52**, 104–115.
- 892 Soloviev, A., Lukas, R. and Hacker, P. (2001) An approach to parameterization of the oceanic turbulent boundary layer in the
893 western Pacific warm pool. *J. Geophys. Res. Oc.*, **106**, 4421–4435.
- 894 Soloviev, A. and Vershinsky, N. (1982) The vertical structure of the thin surface layer of the ocean under conditions of low
895 wind speed. *Deep Sea Res. Part A. Oceanogr. Res. Papers*, **29**, 1437 – 1449.
- 896 Stuart-Menteth, A. C., Robinson, I. S. and Challenor, P. G. (2003) A global study of diurnal warming using satellite-derived sea
897 surface temperature. *J. Geophys. Res. Oc.*, **108**.
- 898 Taylor, P. K. and Yelland, M. J. (2001) The dependence of sea surface roughness on the height and steepness of the waves. *J.*
899 *Phys. Oceanogr.*, **31**, 572–590.

- 900 Teixeira, M. A. C. (2018) A model for the wind-driven current in the wavy oceanic surface layer: Apparent friction velocity
901 reduction and roughness length enhancement. *J. Phys. Oceanogr.*, **48**, 2721–2736.
- 902 Troen, I. B. and Mahrt, L. (1986) A simple model of the atmospheric boundary layer; Sensitivity to surface evaporation. *Bound-
903 Layer Meteorol.*, **37**, 129–148.
- 904 Traskaya, Y. I. and Rybushkina, G. V. (2008) Quasi-linear model of interaction of surface waves with strong and hurricane
905 winds. *Izvest. Atmos. Oc. Phys.*, **44**, 621–645.
- 906 Tsai, W. T., Chen, S. M. and Moeng, C. H. (2005) A numerical study on the evolution and structure of a stress-driven free-
907 surface turbulent shear flow. *J. Fluid Mech.*, **545**, 163–192.
- 908 Ward, B. (2006) Near-surface ocean temperature. *J. Geophys. Res. Oc.*, **111**.
- 909 Ward, B. and Donelan, M. A. (2006) Thermometric measurements of the molecular sublayer at the air-water interface. *Geophys.
910 Res. Lett.*, **33**.
- 911 Ward, B., Wanninkhof, R., Minnett, P. J. and Head, M. J. (2004) SkinDeEP: A profiling instrument for upper-decameter sea
912 surface measurements. *J. Atmos. Oceanic Technol.*, **21**, 207–222.
- 913 Wu, J. (1975) Wind-induced drift currents. *J. Fluid Mech.*, **68**, 49–70.
- 914 – (1983) Sea-surface drift currents induced by wind and waves. *J. Phys. Oceanogr.*, **13**, 1441–1451.
- 915 – (1984) Viscous sublayer below a wind-disturbed water surface. *J. Phys. Oceanogr.*, **14**, 138–144.
- 916 Zeng, X. and Beljaars, A. (2005) A prognostic scheme of sea surface skin temperature for modeling and data assimilation.
917 *Geophys. Res. Lett.*, **32**.

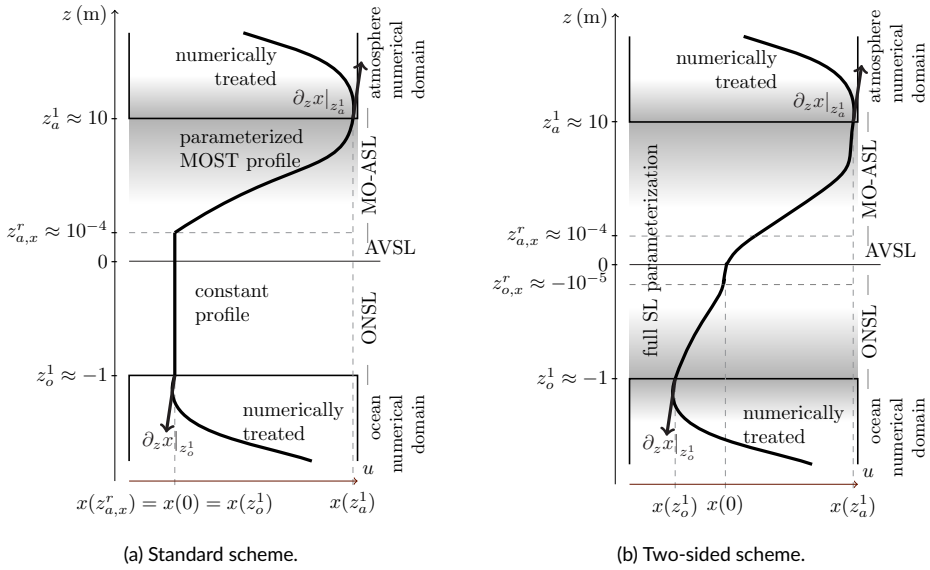


FIGURE 1 Surface layer parameterized schemes for a given transverse variable $x \in \{u, \theta\}$ (velocity or temperature) with arbitrary and nonuniform vertical scales. Grey shadings indicate the layers of MOST validity. (a) is the standard methodology: only a subset of the atmosphere surface layer, the Monin-Obukhov atmosphere surface layer (MO-ASL), is parameterized. Profiles are assumed constant on the atmosphere viscous sublayer (AVSL) and the near-surface layer (ONSL), leading to gradient discontinuities at $z = z_{a,x}^r$ and $z = z_o^1$. (b) is a two-sided parameterization scheme: the full surface layer is parameterized and thus the solution profile is mathematically regular, except at $z = 0$ where the solution gradient can be discontinuous.

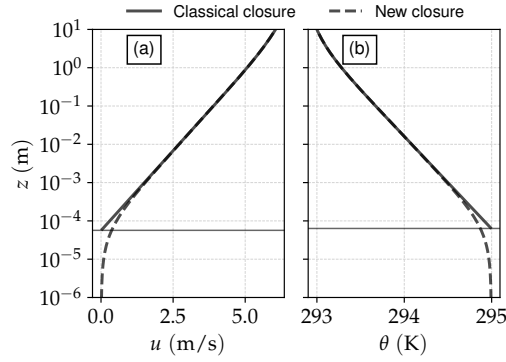


FIGURE 2 Solution profiles for (a) u and (b) θ in the ASL, under unstable stratification, arising from classical dimensionless groups (full plots) and the modified ones (dashed plots) relying on Equations 7 and 9. The roughness height parameterizations and the stability functions are taken from the COARE bulk formula (Fairall et al., 2002). Roughness heights are indicated by thin horizontal lines. Here, $u(z_g^1) = 6$ m/s, $u(0) = 0$ m/s, $\theta(z_g^1) = 293$ K and $\theta(0) = 295$ K. Note the logscaled z -axis.

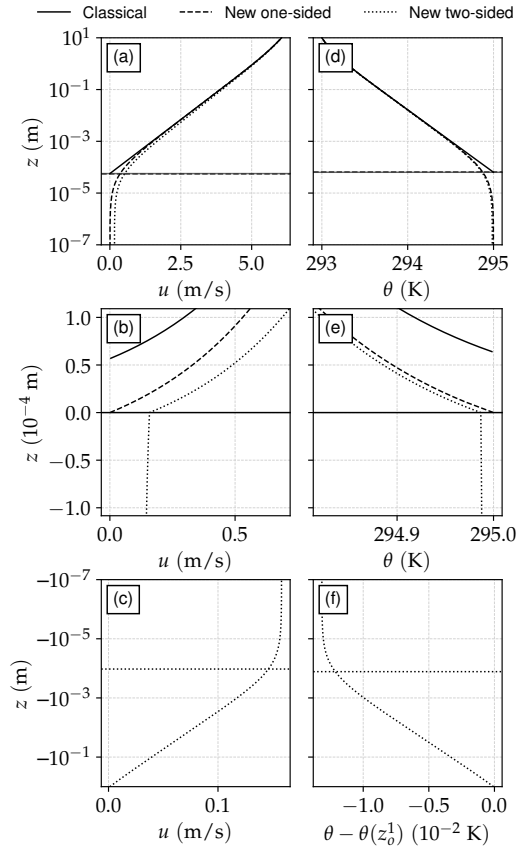


FIGURE 3 Solution profiles for (a),(b),(c) u and (d),(e),(f) θ , arising from classical (full lines), new one-sided (dashed) and cross-interface two-sided (dotted) bulk closures. (a) and (d) (resp. (c) and (f)) represent profiles within the ASL (resp. ONSL), with thin horizontal lines representing the different roughness heights (note the signed logscaled z -axis). (b) and (e) represent solution profiles in the direct vicinity of the ocean-atmosphere interface (note the linear, z -axis). Here, as in Fig. 2, the roughness parameterizations and stability functions are taken from the COARE3.0 algorithm (Fairall et al., 2002). The parameters are $z_0^1 = -1$ m, $z_a^1 = 10$ m, $u(z_a^1) = 6$ m/s, $u(z_0^1) = 0$ m/s, $\theta(z^1) = 293$ K and $\theta(z_0^1) = 295$ K.

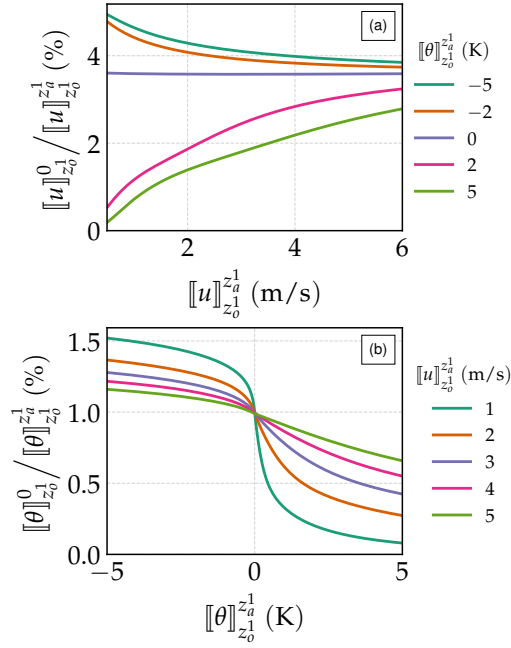


FIGURE 4 Ocean near-surface layer contribution to full surface layer jump for (a) u and (b) θ arising from the regularized two-sided closure Equation 17. Mind the distinct x-axes and legend boxes. Here $z_o^1 = -1$ m and $z_a^1 = 10$ m.

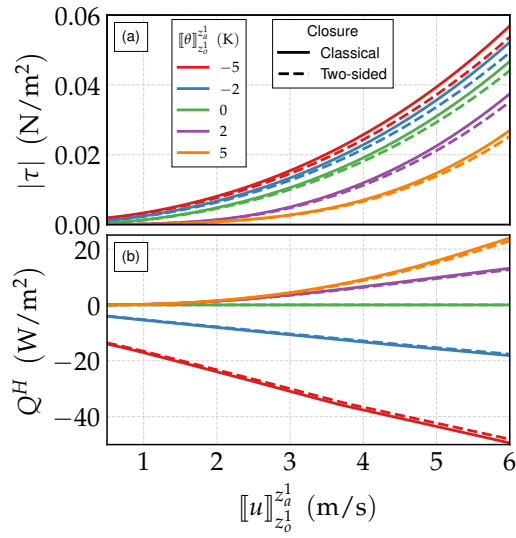


FIGURE 5 Turbulent fluxes (a): wind stress, (b): sensible heat) arising from classical and two-sided bulk closures (solid and dashed lines, respectively). The x-axis is the wind-current surface layer shear $[[u]]_{z_0^1}^{z_a^1}$, and the line colors distinguish different stability regima. Here the bulk formula used is COARE without gustiness nor warm layers parameterizations, with $z_o^1 = -1$ m and $z_a^1 = 10$ m.

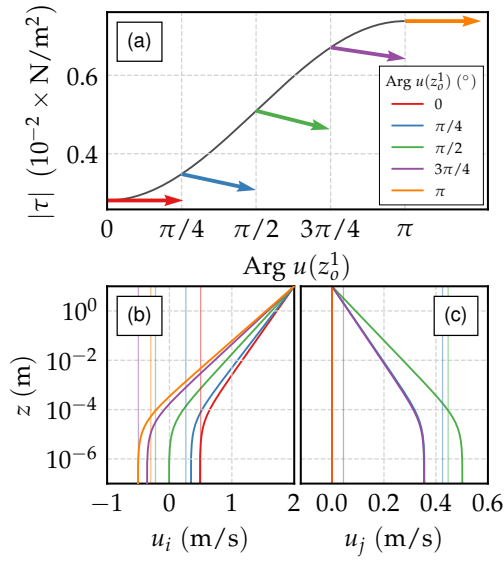


FIGURE 6 Influence of shear direction on surface layer properties. Here a two-sided 2D version of the COARE bulk formula is used with $|u(z_0^1)| = 2$ m/s, $\text{Arg } u(z_0^1) = 0$ (i.e. alignment with the i -direction), $|u(z_0^1)| = 0.5$ m/s, and $\text{Arg } u(z_0^1)$ varying over $[0; \pi]$. (a) displays: $|\tau|$ (black line) and $\text{Arg } \tau$ (colored arrows) for five specific values of $\text{Arg } u(z_0^1)$. With the same color code, (b) and (c) display (u_i, u_j) in the ASL for the same five values of $\text{Arg } u(z_0^1)$ (lines), with $(u_i(z_0^1), u_j(z_0^1))$ specified by the thin vertical lines.

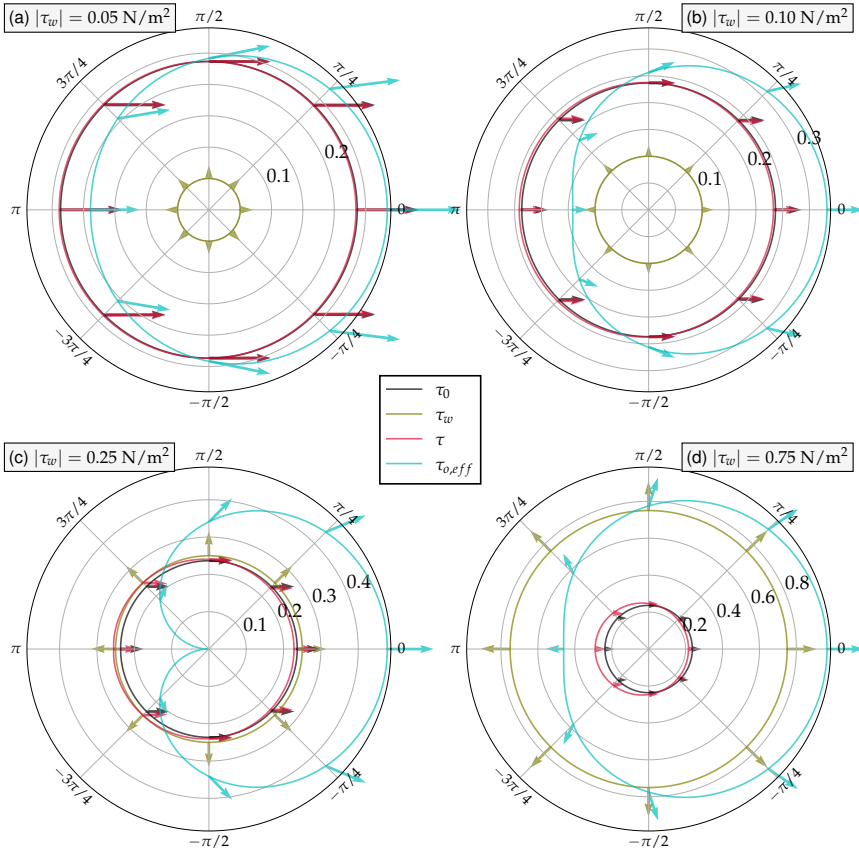


FIGURE 7 Impact of an external wave-induced stress τ_w under various wave directions (angle axis) and norm (radius axis and specified $|\tau_w|$ values) on the wind stress. Plotted here are: wind stresses in the absence of wave (τ_0 , black); wave-induced stress (τ_w , green); wind stress with a τ_w -including closure (τ , red); ocean stress including wave effect ($\tau_{o,eff}$ blue). The norms are represented as lines (in polar coordinates) and the arrows indicate directions. Note that the radii of the polar axis and the scales of the arrow lengths vary in between subfigures. Obtained using a wave-including adapted version of the COARE bulk formula as described in appendix C. Here, $z_o^1 = -1$ m, $z_a^1 = 10$ m, $u(z_a^1) = 12$ m/s, $u(z_o^1) = 0.5$ m/s, $\text{Arg } u(z_a^1) = \text{Arg } u(z_o^1) = 0$, $\theta(z_a^1) = 293$ K, $\theta(z_o^1) = 295$ K.

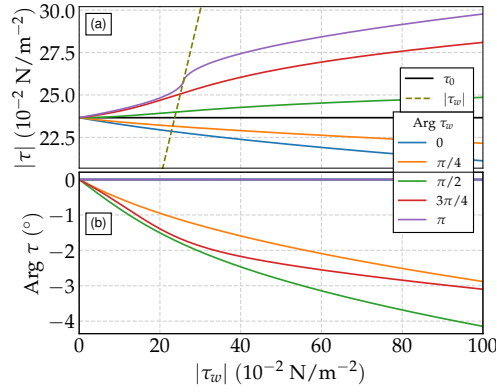


FIGURE 8 Colored lines: wind stress τ ((a): norm, (b) angle) obtained from a wave-including bulk closure, with varying τ_w (norm: x -axis; angle: color code). The black line represents $|\tau_0|$, the wind stress without τ_w . The green dashed line represents $|\tau_w|$, for comparison with $|\tau|$. Here, as in Fig. 7, $u(z_a^1) = 12$ m/s, $u(z_o^1) = 0.5$ m/s, $\text{Arg } u(z_a^1) = \text{Arg } u(z_o^1) = 0$. Note that for readability, the y -axis of (b) is defined in degrees (radians are the angle unit elsewhere).

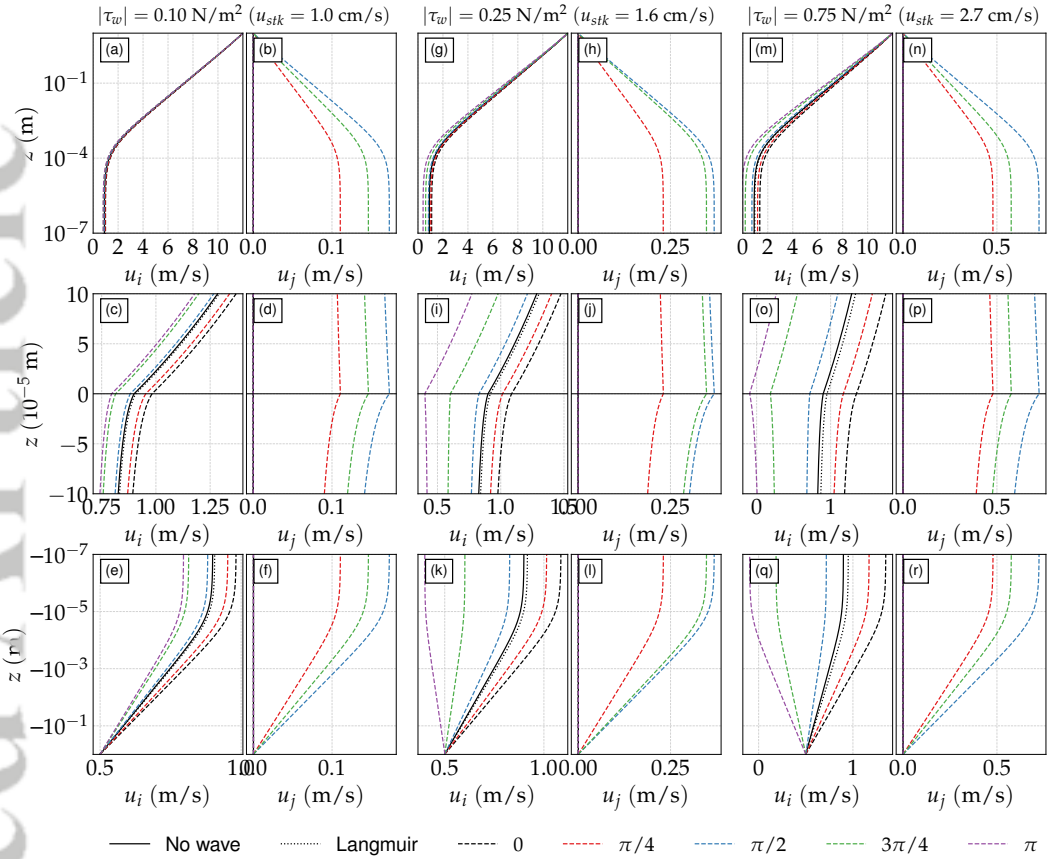


FIGURE 9 Velocity solution profiles on the surface layer for different two-sided closures: two-sided without any wave parameterization (eq. Equation 17, black continuous lines); two-sided with the Langmuir-including closure (eq. Equation 20, black dotted lines); two-sided with τ_w injected in the ocean (as described in Sec. 5.2.2, colored dashed lines). For each solution profiles, u_i and u_j are represented next to each other. Top panels: solutions in the atmosphere SL; middle panels: viscous sublayers; bottom panels: ocean SL. Different values of $|\tau_w|$ are used, specified in top of each pair of columns, with $u_{stk} = \sqrt{|\tau_w|/\rho_o}$ for the Langmuir-including closure. For the wave mass perturbed profiles, different values for $\text{Arg } \tau_w$ are used, specified in the bottom legend. Here, as in Fig. 7, $u(z_a^1) = 12 \text{ m/s}$, $u(z_o^1) = 0.5 \text{ m/s}$, $\text{Arg } u(z_a^1) = \text{Arg } u(z_o^1) = 0$.

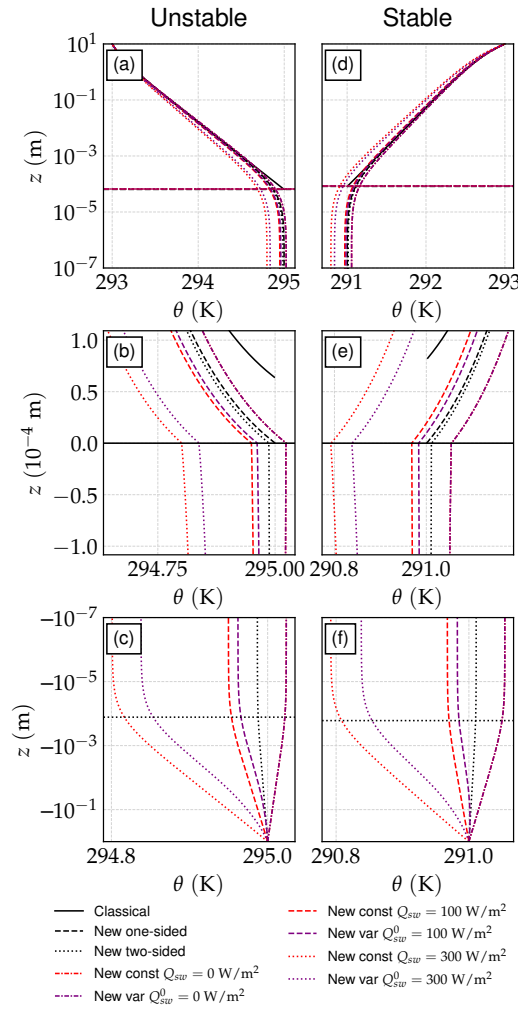


FIGURE 10 θ solution profiles with the SL ((a),(d) atmosphere SL; (b),(e) viscus sublayers; (c),(f) ocean SL), resulting from closures including or excluding the radiative effect. The stratification above is: (a),(b),(c) unstable ($[\theta]_{z_o^1}^{z_a^1} = -2$ K); (d),(e),(f) stable ($[\theta]_{z_o^1}^{z_a^1} = 2$ K). In addition to profiles already represented in Fig. 3, the colored plots represent solution profiles affected by the presence of radiative fluxes: red plots rely on the Equation 25 constant radiation closure, purple ones on the Equation 28 one. On all plots resulting from radiative-inclusive (i.e., colored plots), $Q_{lw}^0 = -50$ W/m² (i.e., the net longwave flux is orientated upwards). Different values for the surface solar radiation Q_{sw}^0 are used, specified in legend. Here, $z_o^1 = -1$ m, $z_a^1 = 10$ m, $[\nu]_{z_o^1}^{z_a^1} = 6$ m/s and $\theta(z_a^1) = 293$ K.

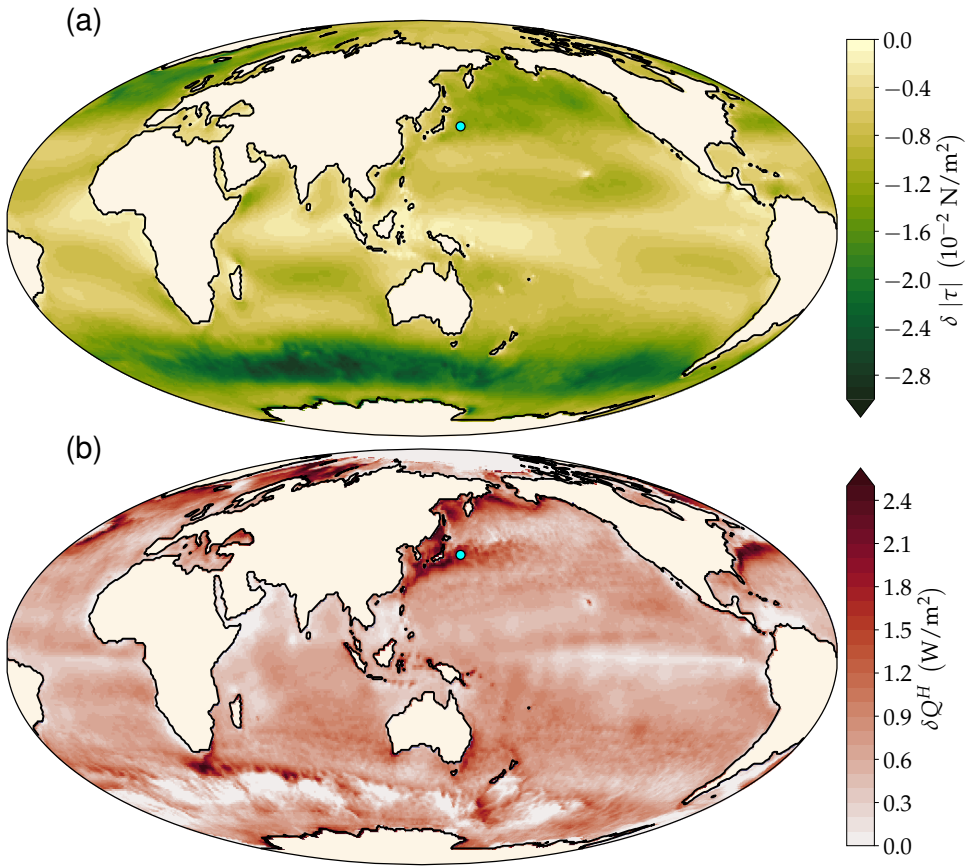


FIGURE 11 Yearly 2006 mean of the differences on turbulent fluxes (a) τ and (b) Q^H between two-sided bulk closures and classical ones, with relative winds (accounting for surface currents). The light blue dot locates the grid cell of the time series shown in Fig. 12.

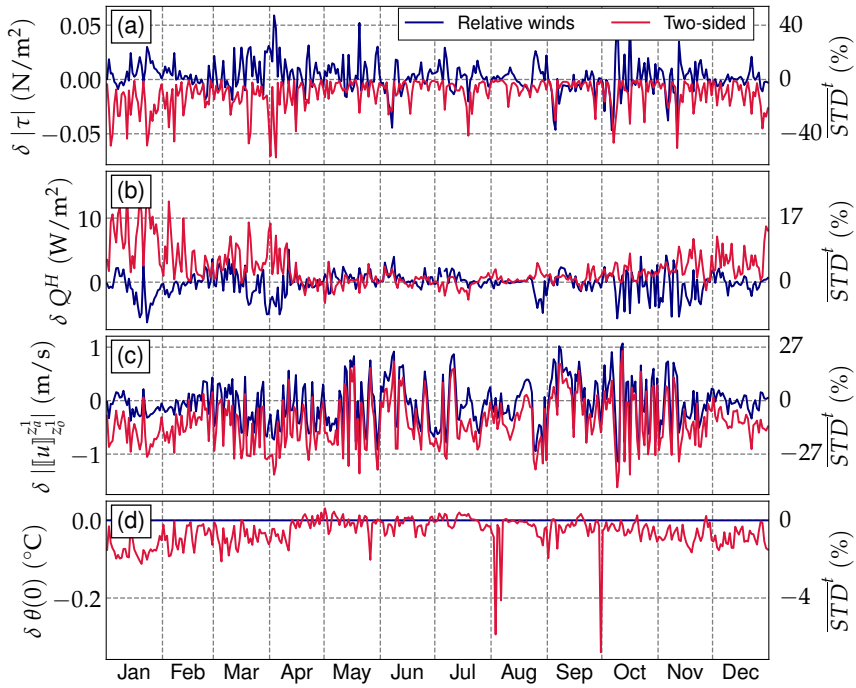


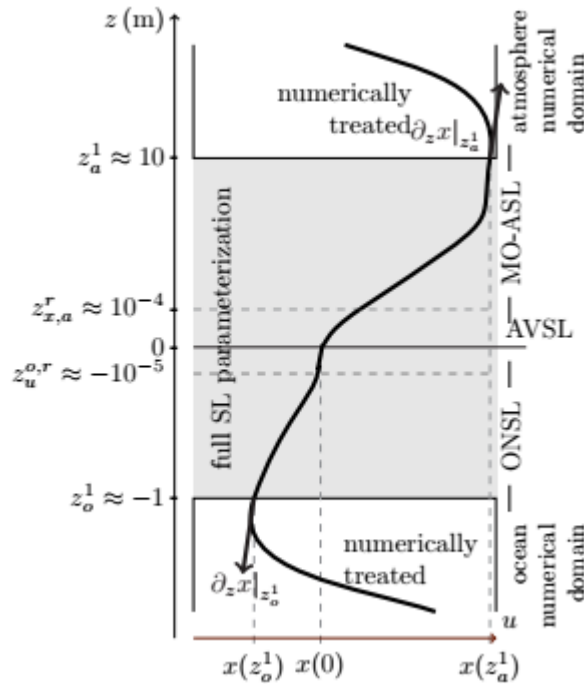
FIGURE 12 2006 time series daily biases from classical relative-winds bulk closures and two-sided ones, with respect to classical absolute-winds bulk closures, at (149.25°E, 36.75°S) (in the Kuroshio current). (a) $\delta |\tau|$, (b) δQ^H , (c) $\delta |[\mathbf{u}]_{z_0}^2|$ and (d) $\delta \theta(z=0)$ from both closures, with the absolute-winds classical bulk closure as reference. Time-wise standard deviations of absolute-winds classical bulk outputs are also given on the right scale.

Symbol	Description	Unit
α	Atmosphere ($\alpha = a$) or ocean ($\alpha = o$)	
u	Winds ($\alpha = a$) or currents ($\alpha = o$)	m/s
θ	Potential temperature	K
$\llbracket x \rrbracket_{z_1}^{z_2}$	$x(z_2) - x(z_1)$	-
τ	Wind stress	N/m ²
Q^H	Sensible heat flux	W/m ²
u_α^*	Momentum turbulent scale	m/s
θ_α^*	Temperature turbulent scale	K
κ	von Kármán constant	
z_α^1	Near-surface vertical level	m
$z_{\alpha,u}^r$	Momentum roughness height ($\alpha = a$) or depth ($\alpha = o$)	m
$z_{\alpha,\theta}^r$	Temperature roughness height ($\alpha = a$) or depth ($\alpha = o$)	m
ϕ_α^m	Momentum stability function	
ϕ_α^h	Scalar stability function	
ψ_α^m	Integrated momentum stability function	
ψ_α^h	Integrated scalar stability function	
λ_u	u_o^*/u_α^* ratio	
λ_θ	$\theta_o^*/\theta_\alpha^*$ ratio	
L_α	Obukhov length	m
ρ_α	Fluid density	kg/m ³
c_α^p	Fluid heat capacity	J kg ⁻¹ K ⁻¹
$\mathcal{K}_{\alpha,u}$	Total fluid momentum diffusivity (viscosity)	m ² /s
$\mathcal{K}_{\alpha,\theta}$	Total fluid temperature diffusivity	m ² /s
\mathcal{K}_α^m	Fluid kinematic viscosity	m ² /s
μ_m	$\mathcal{K}_o^m / \mathcal{K}_\alpha^m$ ratio	
$\mathcal{K}_{\alpha,u}^\nu$	Fluid viscous momentum diffusivity (viscosity)	m ² /s
$\mathcal{K}_{\alpha,\theta}^\nu$	Fluid viscous temperature diffusivity	m ² /s
τ_w	Wave-induced stress	N/m ²

TABLE 1 Non-exhaustive list of symbols used in this paper. Symbols with the α subscript are twofolds: they are defined in both the atmosphere ($\alpha = a$) and the ocean ($\alpha = o$), and are distinct from one medium to the other.

Two-sided turbulent surface layer parameterizations for computing air-sea fluxes

Charles Pelletier*, Florian Lemarié, Eric Blayo, Marie-Noëlle Bouin, Jean-Luc Redelsperger



A framework for extending existing bulk formulae to two-sided ocean-atmosphere versions is presented. Our study relies on parameterizing previously neglected areas of the ocean and atmosphere sublayers, using existing formulations (viscous and Monin-Obukhov derived formulations). The resulting impact on air-sea fluxes is then numerically assessed and discussed.

* corresponding author : charles.pelletier@uclouvain.be